HIGHER-ORDER PETROV-GALERKIN METHODS FOR ANALYSIS OF ANTENNAS

By

Xueying Zhang

Approved:

W. Kyle Anderson
Professor
(Director of Thesis)

James C. Newman
Professor
(Committee Member)

Li. Wang
Assistant Research Professor
(Committee Member)

HIGHER-ORDER PETROV-GALERKIN METHODS FOR ANALYSIS OF ANTENNAS

By

Xueying Zhang

A Thesis
Submitted to the Faculty of the University
of Tennessee at Chattanooga in Partial Fulfillment
of the Requirements of the Degree of Master of Science
in Computational Engineering

The University of Tennessee at Chattanooga
Chattanooga, Tennessee

October 2013

ABSTRACT

A temporally and spatially high-order accurate Petrov-Galerkin finite-element method is applied to the analysis of several antenna configurations. The method obtains numerical solutions of Maxwell's equations in the time domain using implicit time stepping and introduces energy into the domain using a Gaussian pulse to allow frequency-domain parameters to be computed over a range of frequencies with a single time-dependent solution. Verification cases for a monopole antenna and a microstrip patch antenna are used to examine the accuracy of the algorithm. Effects of varying antenna parameters on subsequent performance metrics are discussed based on the results from the simulations. Post-processing procedures are developed to obtain scattering parameters, input impedance and radiation patterns. For verification, the antenna characteristics obtained with the present methodology are compared with the results from two commercial codes. Mesh and time-step refinement studies are also conducted to assess the level of discretization errors in the solutions.

ACKNOWLEDGEMENTS

First of all, I would like to thank Dr. W. Kyle Anderson for his countless hours of advising, reading, encouraging, and patience throughout the entire process. I also thank Dr. James C. Newman for serving on my committee. I would like to express my special thanks to Dr. Li Wang, my committee member, for her patience and courage on me. Finally, I would like to acknowledge and thank Simcenter for providing me academic training and support to the research for the thesis.

TABLE OF CONTENTS

LIST OF TABLES

LIST OF FIGURES

CHAPTER I

INTRODUCTION

Antennas

An antenna is a component of the wireless communication system, and it is designed to radiate or receive electromagnetic waves. The way that an antenna serves a communication system is analogous to the way that eyes serve a human. In the transmitting mode, the antenna is used to convert guided waves within a transmission line to radiated free-space waves; while in the receiving mode, it is used to convert the free-space waves to guided waves. Eyes convert the visual information in the real world to the special information that the brain can receive, and they also convert the information that the brain sends out to emotion expressions. In modern wireless systems, the antenna also acts as a directional device. In this case, the antenna provides enhancement to transmitted or received energy in some directions while restraining it from others. While in the past the antenna technology may have been considered to be secondary, it has become more and more significant in the modern world. The antenna is now one of the most critical components in wireless communication systems.

In 1873, James Clerk Maxwell published his work about unifying the theories of electricity and magnetism, the relations between which were represented through a set of equations: the well-known Maxwell's Equations [1]. In 1886, Professor Heinrich Rudolph Hertz

demonstrated the world's first wireless electromagnetic system between a dipole antenna and a loop antenna in his laboratory [2]. In 1901, Guglielmo Marconi performed a transatlantic transmission from Poldhu in Cornwall, England, to St. John's, Newfoundland, which realized the long-distance signal transmissions for the first time.

Prior to the 1940's, most antenna elements were of the wire type, such as long wires, dipoles, helices and rhombuses. In the 1940's, new elements other than wire related radiating elements were introduced to the antenna technology; open-ended waveguide, slots, horns, reflectors and lenses were developed at that time [3]. In the 1950's, the broadband antennas were developed, which can be applied in a variety of fields such as point-to-point communications, feeds for reflectors and lenses, and the television. In the early 1970's, the microstrip or patch antennas were developed with the advantages of low-profile, low-cost, light-weight and conformability to the surface [4].

Analysis of Antennas

To analyze the characteristics of an antenna, the electric and magnetic fields radiated by the elements need to be obtained first. Based on the fields, a number of parameters that characterize the performance of the antenna system can be found.

Traditionally, the antenna problems were solved analytically and experimentally. Only a few idealized antenna geometries can be solved analytically by Maxwell's equations. For the antennas that could not be solved analytically, the experimental methods were applied. The scattering parameters of an antenna can be obtained by a network analyzer, and the radiation

pattern can be obtained by a field scanner through experiments in an anechoic chamber. However, the cost of designing an antenna by experimental methods was too high, although this is not to negate the importance of experimental methods which are still used today for the verification of antenna characteristics.

In the early 1960's, numerical methods were introduced to antenna technology which provides good predictions and high performances. Numerical simulations help shorten the design cycle and have the capability to analyze complex antennas. Numerical simulations cost much less than experiments and can be applied in exploration of larger design space. However, numerical simulations still have some challenges. For example, improper use of a numerical solution would yield either a poor or a completely erroneous design.

Numerical Methods for Simulations of Antennas

A variety of numerical methods are applied in computational electromagnetics and they are mainly based on the finite-difference time-domain method, the method of moments, the finite-volume method and the finite-element method.

In the 1960's, Yee invented the finite-difference time-domain method (FDTD) that solved Maxwell's equations discretized on structured grids directly in the time domain [5]. Within one time-domain calculation, the broadband solution can be obtained through the Fourier transform. The method is efficient as no matrix solutions need to be calculated and also simple in implementation and grid generation. In addition, the method has the capability for anisotropic and inhomogeneous materials. Despite the advantages mentioned above, FDTD suffers from

some limitations. The major limitation for the finite-difference time-domain method is its capability to model complex geometrical structures such as curved surfaces and devices with a widely varying range of geometric scales. Nevertheless, the finite-difference time-domain method is still a popular choice for computational electromagnetics, and a variety of methods are developed based on FDTD. For instance, the widely used simulation software CST Microwave Studio [6] is a Finite Integral Technique (FIT) solver, which is basically FDTD with integration instead of differentiation. CST MICROWAVE STUDIO®(CST MWS) is a specialist tool for the 3D EM simulation of high frequency components. CST MWS enables the fast and accurate analysis of high frequency (HF) devices such as antennas, filters, couplers, planar and multi-layer structures and SI and EMC effects. The patch antennas in this thesis are simulated by CST(in short for CST MWS) for comparison.

In 1968, the method of moments(MoM) for electromagnetic analysis was introduced by Harrington in his book [7], and then it was widely applied in antenna analysis [8, 9]. The method of moments is based on the formulation of integral equations in terms of Green's functions as the fundamental solution to Maxwell's equations. The method is efficient for antennas with structures of layered substrates, such as microstrip patch antennas which will be discussed in this thesis, and also for antennas with bulk homogeneous dielectrics, such as dielectric resonator antennas. This is because the effect of the dielectrics can either be accounted for by a special Green's function or be modeled by equivalent electric and magnetic surface currents [10]. However, the method of moments suffers from some shortcomings such as the capability of modeling complex antennas designed with complex materials that may be anisotropic and inhomogeneous.

The finite-volume method is another approach applied in computational electromagnetics. Maxwell's equations in this form have mathematical similarities with the compressible Euler equations from fluid dynamics. These relationships are taken advantage of by the finite-volume method in solving the Maxwell's equations [11, 12]. However, the second-order accuracy determined by the discretization of the spatial derivatives in this method is not sufficient to solve problems requiring higher-order accuracy such as high-frequency applications and electrically large structures.

The finite-element method was introduced to computational electromagnetics by Jin in his book [13]. Though its application in electromagnetics is not as widely as FDTD and MoM are, it has many advantages such as the capability for modeling both complex structures and materials. The method can accurately model curved surfaces and complex structures by applying unstructured meshes with curvilinear triangular and tetrahedral elements. The finite element method is suitable for parallel computations when combined with domain-decomposition algorithms. Although the method requires solving a large matrix equation, its solution can be obtained efficiently with the use of advanced solvers. The Maxwell's equations are solved by the finite element method with a weighting function added to the governing equations as a factor and integrated over the volume. The most popular implementation of this method for electromagnetic simulations is to solve for either the electric or magnetic fields through the wave equation. The other field variables are obtained in a post-processing step by numerical differentiation, the order of truncation error of which is one order less than the former one. The commercial simulation software HFSS [14] is based on the finite element method. The High Frequency Structure Simulator (HFSS™) is a software tool for 3D full-wave electromagnetic field simulations. HFSS

provides E- and H-fields, currents, S-parameters, and near and far radiated field results. The models discussed in this thesis are simulated in HFSS for comparison.

Petrov-Galerkin Methods for Time-Domain Simulations on Antennas

Maxwell's equation can be cast in both the time domain and the frequency domain, and consequently the numerical simulation can be applied in either the time domain or the frequency domain. The frequency-domain numerical method is highly suitable for scattering analysis, where the main concern is the scattering due to plane waves from many incident directions. The reason is that the matrix equation in the frequency-domain method is solved for each frequency, where different excitations can be applied. The time-domain numerical method is well suited for antenna analysis where the main concern is a solution over a broad frequency band for one or a few excitations. The broadband solution can be obtained through the Fourier transform in one time-domain calculation. In addition, the time-domain methods have the capability for modeling nonlinear components, devices and media in an antenna system, which is a unique strength over frequency-domain methods.

Petrov-Galerkin finite element methods are applied to solve Maxwell's equations in the present work [15]. The method is highly suitable for analysis and design of large electromagnetic structures. It has the capability of dealing with high-order spatial discretization which helps represent complex geometries accurately. The field variables are stored at the vertices of the tetrahedrons in single-valued form, hence reducing the number of unknowns to be computed.

The Petrov-Galerkin method has been successfully applied in computational fluid dynamics [16], and the computation electromagnetics will be an attractive field for the method to explore.

In this thesis, the Simcenter's in-house code using the Fully Unstructured Adaptive Finite Element method (FUNSAFE) is applied in analysis of the antennas. The antennas are simulated in the time domain with excitation of a Gaussian pulse to obtain frequency-based parameters. Two kinds of basic antennas are discussed consisting of a monopole antenna and a microstrip patch antenna. The effects of antenna parameters on antenna characteristics are discussed according to the simulations results. The simulation results of antenna characteristics including the scattering parameters, input impedance and radiation pattern are compared with the results of HFSS and CST for verification. Convergence tests are also operated on the antenna cases for assessment of the computational accuracy.

CHAPTER II

PETROV-GALERKIN METHODS FOR ELECTROMAGNETIC SIMULATIONS AND FUNDAMENTALS OF ANTENNAS

Petrov-Galerkin Methods for Electromagnetic Simulations

Governing Equation

Maxwell's equations are the basic laws in electromagnetics that describe electric and magnetic phenomena at the macroscopic level. The general form of time-varying Maxwell equations can be expressed as:

$$\nabla \times E = -\frac{\partial B}{\partial t} - M \tag{2.1}$$

$$\nabla \times H = \frac{\partial D}{\partial t} + J \tag{2.2}$$

$$\nabla \cdot B = 0 \tag{2.3}$$

$$\nabla \cdot D = \rho_c \tag{2.4}$$

where E is the electric field, H is the magnetic field, D is the electric flux density, B is the magnetic flux density, M is the (fictitious) magnetic current density, J is the electric current density and ρ_c is the electric charge density.

The currents M and J and the electric charge density ρ_c are the sources of the electromagnetic field. In a source-free region, M, J and ρ_c are all zero, which is the situation we

will be discussed below. The flux densities and the field intensities have the following relationships:

$$B = \mu H \tag{2.5}$$

$$D = \varepsilon E \tag{2.6}$$

where μ is the permeability and ε is the permittivity. The governing equations are rewritten in a divergence form as follows:

$$\frac{\partial \boldsymbol{Q}}{\partial t} + \nabla \cdot \boldsymbol{F}(\boldsymbol{Q}) = 0 \tag{2.7}$$

$$\boldsymbol{Q} = (D_x, D_y, D_z, B_x, B_y, B_z)^T \tag{2.8}$$

$$\boldsymbol{F} = \hat{\imath}\boldsymbol{f} + \hat{\jmath}\boldsymbol{g} + \hat{k}\boldsymbol{h} \tag{2.9}$$

$$\boldsymbol{f} = (0, H_z, -H_y, 0, -E_z, E_y)^T \tag{2.10}$$

$$\boldsymbol{g} = (-H_z, 0, H_x, E_z, 0, -E_x)^T \tag{2.11}$$

$$\boldsymbol{h} = \left(H_y, -H_x, 0, -E_y, E_x, 0\right)^T \tag{2.12}$$

The equations above can be written in the differential form as:

$$\frac{\partial}{\partial t}\begin{bmatrix} D_x \\ D_y \\ D_z \\ B_x \\ B_y \\ B_z \end{bmatrix} + \frac{\partial}{\partial x}\begin{bmatrix} 0 \\ B_z/\mu \\ -B_y/\mu \\ 0 \\ -D_z/\varepsilon \\ D_y/\varepsilon \end{bmatrix} + \frac{\partial}{\partial y}\begin{bmatrix} -B_z/\mu \\ 0 \\ B_x/\mu \\ D_z/\varepsilon \\ 0 \\ -D_x/\varepsilon \end{bmatrix} + \frac{\partial}{\partial z}\begin{bmatrix} B_y/\mu \\ -B_x/\mu \\ 0 \\ -D_y/\varepsilon \\ D_x/\varepsilon \\ 0 \end{bmatrix} = 0 \tag{2.13}$$

Numerical Solution

The Petrov-Galerkin method is applied in FUNSAFE to solve the Maxwell's equations in both time-domain and frequency-domain. The Petrov-Galerkin method is formulated as a weighted residual method, which can be expressed in the following form:

$$\iiint_{\Omega}[\emptyset]\left(\frac{\partial \boldsymbol{Q}}{\partial t}+\nabla\cdot\boldsymbol{F}\right)\partial\Omega=0 \tag{2.14}$$

where $\emptyset$ is a weighting function given by:

$$[\emptyset]=N[I]+\left(\frac{\partial N}{\partial x}[A]+\frac{\partial N}{\partial y}[B]+\frac{\partial N}{\partial z}[C]\right)[\tau]=N[I]+[P] \tag{2.15}$$

Streamlined Upwind Petrov-Galerkin(SUPG) method is used in defining the weighting function [17]. Here, $N[I]$, the first part of $\emptyset$, can be represented as:

$$N=\sum_{i=1}^{n}N_i c_i \tag{2.16}$$

which is composed of a linear combination of the basis functions and defines the variables within the element. Also, c_i in the equation above represent arbitrary constants. $[P]$, the second part of the weighting function, is a stabilizing term that dissipates odd-even point decoupling along preferential directions. $[\tau]$ represents the stabilization matrix and can be obtained using the following definitions [18]

$$[\tau]^{-1}=\sum_{k=1}^{n}\left|\frac{\partial N_k}{\partial x}[A]+\frac{\partial N_k}{\partial y}[B]+\frac{\partial N_k}{\partial z}[C]\right| \tag{2.17}$$

$$\left|\frac{\partial N_k}{\partial x}[A]+\frac{\partial N_k}{\partial y}[B]+\frac{\partial N_k}{\partial z}[C]\right|=[T][|\Lambda|]\,[T]^{-1} \tag{2.18}$$

where $[T]$ and $[\Lambda]$ are the right eigenvectors and eigenvalues of the matrix on the left side of Eq. (2.18) respectively, and $[T]^{-1}$ represents the inverse of $[T]$.

In the Petrov-Galerkin finite-element approach, field variables are assumed continuous across element boundaries. Hence, data is stored at the vertices and faces of the elements as a single-valued form. Within each element, the solution is assumed to vary according to a linear combination of polynomial basis functions given by:

$$\boldsymbol{Q}_h=\sum_{i=1}^{n}N_i\boldsymbol{Q}_i \tag{2.19}$$

In this equation, $\boldsymbol{Q}_h$ represent the approximated variables within each element dependent on $\boldsymbol{Q}_i$ and N_i, $\boldsymbol{Q}_i$ is the corresponding data at each node of the element, and each N_i represents a basis function, where the basis functions of Eq. (2.16) come from.

As a result, the weak statement above may be expressed as:

$$\oiiint_{\Omega}\left(N\left\{\frac{\partial \boldsymbol{Q}}{\partial t}\right\}-\boldsymbol{F}\cdot\nabla N\right)\partial\Omega+\oiiint_{\Omega}[P]\left(\frac{\partial \boldsymbol{Q}}{\partial t}+\nabla\cdot\boldsymbol{F}\right)\partial\Omega+\oint_{\Gamma}N\boldsymbol{F}\cdot\hat{n}\partial\Gamma=0 \quad (2.20)$$

To be noticed, the surface integral needs only to be evaluated on the boundaries of the domain where appropriate boundary conditions are weakly enforced by incorporating them into the surface integral. Because the field variables are assumed to vary continuously in the interior of the domain, the surface integral typically vanishes on the boundaries of the interior elements.

In the Petrov-Galerkin scheme, the domain of interest is discretized into a series of non-overlapping elements. For three-dimensional applications in the present work, the tetrahedral elements are applied. The tetrahedrons within the computational mesh are mapped to parent tetrahedrons which have coordinates in non-dimensional (x', y', z') space. Gaussian quadrature rules are used in evaluating the volume and surface integrals. In evaluating the volume integrals, a function integrated over a tetrahedron can be expressed as:

$$\oiiint_{\Omega} f(x,y,z)\partial\Omega=\sum_{i=1}^{N_{gauss}} f_i(x(x',y',z'),y(x',y',z'),z(x',y',z'))W_iJ \quad (2.21)$$

where (x', y', z') are Gauss points, W_i are Gauss weights, and J is the Jacobian.

In evaluating the surface integrals, a function integrated over a triangle can be expressed as:

$$\iint_{\Gamma} f(x,y,z)\partial\Gamma=\sum_{i=1}^{N_{gauss}} f_i(x(x',y'),y(x',y'),z(x',y'))W_iJ \quad (2.22)$$

where (x', y') are Gauss points, W_i are Gauss weights, and J is the Jacobian.

For polynomial representations of the dependent variables of p, formulas for integrating polynomials of order 2p are used in evaluating volume integrals while formulas for integrating polynomials of order 2p+1 are used in evaluating surface integrals [19].

For the antenna cases in the present work, the computational domain includes multiple materials of differing permittivities. In this case, the surface integral must be evaluated at the interface between the materials, because there will be discontinuous jumps in the tangential components of flux densities across the interface [20, 21]. Duplicate nodes are introduced in solving this problem and they are created on either side of the interface. The flux on the boundary between different materials is determined using a Riemann flux function given by:

$$\boldsymbol{F}(\boldsymbol{q}_L, \boldsymbol{q}_R) \cdot \hat{n} = \frac{1}{2}[\boldsymbol{F}(\boldsymbol{q}_L) + \boldsymbol{F}(\boldsymbol{q}_R) - [\tilde{T}][\tilde{\Lambda}][\tilde{T}][\tilde{M}]\Delta\boldsymbol{q}] \tag{2.23}$$

where $[\tilde{T}]$, $[\tilde{\Lambda}]$, and $[\tilde{M}]$ represent average values and

$$\boldsymbol{q} = (E_x, E_y, E_z, H_x, H_y, H_z)^T \tag{2.24}$$

And the difference in values across the interface $\Delta\boldsymbol{q}$ can be expressed as:

$$\Delta\boldsymbol{q} = \boldsymbol{q}_R - \boldsymbol{q}_L \tag{2.25}$$

Also, the matrix M is given by:

$$[M] = \left[\frac{\partial \boldsymbol{Q}}{\partial \boldsymbol{q}}\right] \tag{2.26}$$

Here, the flux densities Q are computed at each mesh point during the simulations. The ideas above come from the flux-difference-splitting method in the fluid dynamic applications [22].

Boundary Conditions

The boundary conditions are weakly enforced by modifying the fluxes when evaluating Eq. (2.20). Four kinds of boundary conditions will be introduced below: perfect electric conducting (PEC) boundary conditions, material jump boundary conditions, Silver-Muller boundary conditions [23], and Dirichlet boundary conditions.

For PEC boundary conditions, the flux vector is given by:

$$\boldsymbol{F} = \hat{\imath}\boldsymbol{f} + \hat{\jmath}\boldsymbol{g} + \hat{k}\boldsymbol{h} \tag{2.27}$$

where

$$\boldsymbol{f} = \begin{bmatrix} 0 \\ B_z/\mu \\ -B_y/\mu \\ 0 \\ 0 \\ 0 \end{bmatrix}, \boldsymbol{g} = \begin{bmatrix} -B_z/\mu \\ 0 \\ B_x/\mu \\ 0 \\ 0 \\ 0 \end{bmatrix}, \boldsymbol{h} = \begin{bmatrix} B_y/\mu \\ -B_x/\mu \\ 0 \\ 0 \\ 0 \\ 0 \end{bmatrix} \tag{2.28}$$

Then, the flux normal to the boundary surface in the interior can be expressed as:

$$\boldsymbol{F} \cdot \hat{n} = \begin{bmatrix} -n_y H_z + n_z H_y \\ n_x H_z - n_z H_x \\ -n_x H_y + n_y H_x \\ 0 \\ 0 \\ 0 \end{bmatrix} \tag{2.29}$$

For material jump boundary conditions (such as port boundaries and interface between different materials), the flux is determined by Eq. (2.23) using the Riemann flux solver. For port boundaries, the data on the interior side of the interface is obtained from the field variables, and the data on the exterior side of the interface is obtained using a driving wave.

For Silver-Muller boundary conditions, the flux can be derived from the following equation [23]:

$$(\boldsymbol{E} - c\boldsymbol{B} \times \boldsymbol{n}) \times \boldsymbol{n} = e^* \times \boldsymbol{n} \tag{2.30}$$

or, in a similar way,

$$(c\boldsymbol{B} + \boldsymbol{E} \times \boldsymbol{n}) \times \boldsymbol{n} = cb^* \times \boldsymbol{n} \tag{2.31}$$

where (***E***,***B***) denotes the electromagnetic field, c is the speed of light and **n** is the unit outside normal to the boundary. For the cases that the plane wave propagates normally to the boundary, e^* and b^* are set to zero, which is applied in FUNSAFE simulations.

For Dirichlet boundary conditions, the values of $\boldsymbol{q}$ at each node on the boundary are set to the desired values. In the present work of antenna simulations, Dirichlet free stream boundary conditions are applied at the end of perfectly-matched layer (PML). When needed, the PML approach in reference [24] is used for time-domain simulations.

Scattering Parameters and Input Impedance

Scattering Parameters

Scattering parameters describe the input-output relationship between ports in an electrical system. Regarding a typical two-port network, the scattering matrix shows the relationship between the outgoing waves b_1, b_2 and incoming waves a_1, a_2 that are incident at the two ports:

$$\begin{bmatrix} b_1 \\ b_2 \end{bmatrix} = \begin{bmatrix} S_{11} & S_{12} \\ S_{21} & S_{22} \end{bmatrix} \begin{bmatrix} a_1 \\ a_2 \end{bmatrix}, S = \begin{bmatrix} S_{11} & S_{12} \\ S_{21} & S_{22} \end{bmatrix} \tag{2.32}$$

The matrix elements, S_{11}, S_{12}, S_{21}, S_{22} are referred to as the scattering parameters. The parameters S_{11} and S_{22} represent reflection coefficients, and parameters S_{21} and S_{12} represent transmission coefficients.

In practice, the most commonly quoted parameter in regards to antennas is S_{11}. S_{11} represents how much power is reflected from the antenna. From this reason, S_{11} is also known as

reflection coefficient(sometimes written as Γ). The relationship among S_{11}, return loss and input impedance will be discussed later.

Input Impedance

Input impedance is the impedance presented by an antenna at its terminals [25]. In this thesis, the antennas discussed are all fed by a coaxial cable, and the impedance represents the ratio of voltage and current presented at the coax port. Later in Chatper III, the details of the procedure to obtain the input impedance will be discussed.

Relationship among S_{11}, Return Loss and Input Impedance

Return loss is an important factor of antennas which describes the reflection characteristics of antennas. The definition of return loss is given by:

$$RL(dB) = -20log_{10}|\Gamma| \tag{2.33}$$

where Γ, the reflection coefficient, represents the ratio of the reflected wave V_r to the incident wave V_i :

$$\Gamma = \frac{V_r}{V_i} \tag{2.34}$$

When the source and load impedances are known values, the reflection coefficient is given by:

$$\Gamma = \frac{Z_L - Z_S}{Z_L + Z_S} \tag{2.35}$$

where Z_S is the impedance toward the source and Z_L is the impedance toward the load.

For the coaxial-line fed antennas, Z_S represents the characteristic impedance of the coax which is determined by the dimensions of coaxial cable only, and Z_L represents the input impedance of the antenna. From the equations above, return loss can also be represented by:

$$RL(dB) = -20log_{10}\left|\frac{V_r}{V_i}\right| = -20log_{10}\left|\frac{Z_L - Z_S}{Z_L + Z_S}\right| \quad (2.36)$$

Return Loss can be also represented as:

$$RL(dB) = -10log_{10}\left|\frac{Re(P_{re})}{Re(P_{in})}\right| \quad (2.37)$$

Here, P_{re} is the reflection power at the port, and P_{in} is the incident power at the port.

To be noticed, when S_{11} is applied in describing antenna characteristics, it refers to the decibel format instead of complex format in most cases. Combined with Eq. (2.37), the formula applied in calculation of S_{11}(dB) can be expressed as:

$$S_{11}(dB) = -RL(dB) = 10log_{10}\left|\frac{Re(P_{re})}{Re(P_{in})}\right| \quad (2.38)$$

The formula above is applied in the FUNSAFE code to get S_{11} of the antennas.

Radiation Pattern

Definition

The Radiation Pattern of an antenna is the special distribution of a quantity which characterized the electromagnetic field generated by an antenna [26]. In most cases, the radiation pattern is determined in the far-field region and is represented as a function of the directional coordinates. The radiation pattern indicates the radiating and receiving properties of an antenna

in the far-field on angular dependence, in which radiation properties include power flux density, radiation intensity, directivity, phase, polarization, and field strength.

In most cases, the patterns are normalized with respect to their maximum value. In addition, the patterns are usually plotted on a logarithmic scale or more commonly in decibels (dB). A typical antenna pattern has a main lobe, sidelobes, minor lobes, a backlobe, and several nulls in a $\varphi = const.$ plane, φ is the azimuthal angle in spherical coordinated, as shown in Fig. 1. A logarithmic scale is desirable since it can accentuate in more details the low-value parts in the pattern, such as the minor lobes.

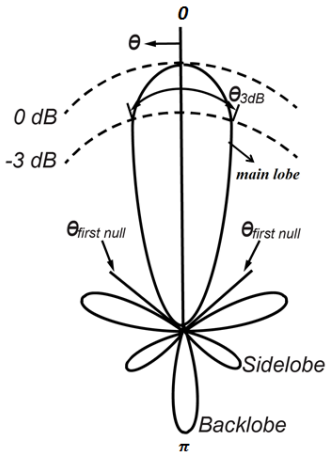

Figure 1 Antenna Pattern in Plane $\varphi = const.$

If the pattern cut of an antenna is in x-z plane ($\varphi = 0$) parallel to the E field vector, the corresponding pattern is called an E-plane pattern. Alternatively, if the pattern is given in y-z plane ($\varphi = \frac{\pi}{2}$) parallel to the H field polarization, it is referred to as an H-plane pattern.

There are many types of antenna radiation patterns, but the most common ones are: Omnidirectional Pattern, Pencilbeam Pattern, Fan beam Pattern and Shaped beam Pattern. The

Omnidirectional pattern is the most popular in communication and broadcast applications. The omnidirectional antenna radiates equally in all horizontal directions, while varying with elevation angles [26]. The monopole antenna later discussed in Chapter III is an omnidirectional antenna.

Near to Far Field Transform

To get antenna radiation characteristics, a formal simplification of the problem is to replace the antenna by equivalent sources on an arbitrary surface S enclosing it according to the equivalence principle [27]. These equivalent sources reproduce the radiated fields of the antenna, which can be assumed as radiating in homogeneous space. For a particular antenna configuration, the exact determination of equivalent sources can be realized through knowledge of the true field distribution on S according to Huygens' principle [27]. For convenience, vector potentials are applied in obtaining the radiating characteristics. The details of calculating antenna radiation characteristics are discussed below.

Huygens' and Equivalence Principles

Numerical simulation is used to compute approximate solutions for practical configurations since the exact solutions of Maxwell's equation are typically unavailable. To simplify the electromagnetic antenna problems, the equivalence principle is employed. According to the equivalence principle, the antenna configuration can be replaced by the equivalent electromagnetic sources located on the surface of a volume enclosing the antenna

configuration. These sources are usually radiating in a homogeneous solution space, and then the corresponding fields can be calculated by evaluating the radiation integrals.

Huygens' principle provides a straightforward way to construct equivalent sources. Huygens' principle states that the field solution in a region V is completely determined by the tangential fields over the surface S enclosing V. The corresponding electric and magnetic equivalent surface current densities are given by:

$$\mathbf{J} = \hat{n} \times \boldsymbol{H} \tag{2.39}$$

$$\mathbf{M} = -\hat{n} \times \boldsymbol{E} \tag{2.40}$$

where both **J** and **H** are expressed in amperes per meter(A/m), and **M** and **E** are expressed in volts per meter(V/m) [28]. By applying Huygens' principle, the antenna radiation pattern can be computed from a near-field surface integral based on the equivalent currents located on the surfaces within the mesh.

Calculation of Far-Field Radiation Characteristics through Vector Potential

The vector wave equation related to the vector potential A is given by:

$$\nabla^2 \mathrm{A} + \beta^2 \mathrm{A} = -\mu \, \mathrm{J} \tag{2.41}$$

where J represents the electric current density and the related electric and magnetic fields can be expressed as a function of A:

$$E_A = -j\omega A - j\frac{1}{\omega\mu\varepsilon}\nabla(\nabla \cdot A) \tag{2.42}$$

$$H_A = \frac{1}{\mu}\nabla \times A \tag{2.43}$$

Alternatively, the vector wave equation related to the vector potential F is given by:

$$\nabla^2 \mathrm{F} + \beta^2 \mathrm{F} = -\varepsilon \mathrm{M} \tag{2.44}$$

where M represents the magnetic current density and the related magnetic field can be expressed as a function of F:

$$E_F = -\frac{1}{\varepsilon}\nabla \times F \tag{2.45}$$

$$H_F = -j\omega F - j\frac{1}{\omega\mu\varepsilon}\nabla(\nabla \cdot F) \tag{2.46}$$

The fields radiated by antennas of finite dimensions in the far-zone are spherical waves. For these radiators, a general solution to the vector wave equation (2.41) in spherical components should have the general form as:

$$A = \hat{a}_r A_r(r,\theta,\varphi) + \hat{a}_\theta A_\theta(r,\theta,\varphi) + \hat{a}_\varphi A_\varphi(r,\theta,\varphi) \tag{2.47}$$

According to Eqs. (2.42-2.43) and neglecting high-order terms of $1/r^n$, the radiated E and H fields have only θ and φ components which can be expressed as:

$$E_r \cong 0 \tag{2.48}$$

$$E_\theta \cong -j\omega A_\theta \tag{2.49}$$

$$E_\varphi \cong -j\omega A_\varphi \tag{2.50}$$

$$H_r \cong 0 \tag{2.51}$$

$$H_\theta \cong +j\frac{\omega}{\eta}A_\varphi \tag{2.52}$$

$$H_\varphi \cong -j\frac{\omega}{\eta}A_\theta \tag{2.53}$$

Similarly, the far-zone fields related to potential F can be expressed as according to Eqs. (2.45-2.46):

$$H_r \cong 0 \tag{2.54}$$

$$H_\theta \cong -j\omega F_\theta \tag{2.55}$$

$$H_\varphi \cong -j\omega F_\varphi \tag{2.56}$$

$$E_r \cong 0 \tag{2.57}$$

$$E_\theta \cong -j\omega\eta F_\varphi \tag{2.58}$$

$$E_\varphi \cong +j\omega\eta F_\theta \tag{2.59}$$

The corresponding far-zone E-field and H-field components are orthogonal to each other and form TEM mode fields.

For an observation point in the far field($\beta r \gg 1$), the radial distance R from any point on the source or scatterer to the observation point can be assumed to be parallel to the radial distance r from the origin to the observation point. Approximately, the relationship between R and r can be represented as:

$$R = \begin{cases} r - r'cos\varphi & \text{for phase variations} \\ r & \text{for amplitude variations} \end{cases} \tag{2.60}$$

According to the equation above, the solution of vector potential wave equation (2.41) and (2.42) can be rewritten as:

$$\mathrm{A} = \frac{\mu}{4\pi}\iint_S \mathrm{J}_s \frac{e^{-j\beta R}}{R} ds' \cong \frac{\mu e^{-j\beta r}}{4\pi r} N \tag{2.61}$$

$$\mathrm{F} = \frac{\varepsilon}{4\pi}\iint_S \mathrm{M}_s \frac{e^{-j\beta R}}{R} ds' \cong \frac{\varepsilon e^{-j\beta r}}{4\pi r} L \tag{2.62}$$

where

$$\mathrm{N} = \iint_S \mathrm{J}_s e^{j\beta r' cos\varphi} ds' \tag{2.63}$$

$$\mathrm{L} = \iint_S \mathrm{M}_s e^{j\beta r' cos\varphi} ds' \tag{2.64}$$

Using Eqs. (2.48-2.59), the E-field and H-field in the far field can be written as:

$$E_r \cong 0 \tag{2.65}$$

$$E_\theta \cong (E_A)_\theta + (E_F)_\theta = -j\omega[A_\theta + \eta F_\varphi] \tag{2.66}$$

$$E_\varphi \cong (E_A)_\varphi + (E_F)_\varphi = -j\omega[A_\varphi - \eta F_\theta] \tag{2.67}$$

$$H_r \cong 0 \tag{2.68}$$

$$H_\theta \cong (H_A)_\theta + (H_F)_\theta = +j\frac{\omega}{\eta}[A_\varphi - \eta F_\theta] \tag{2.69}$$

$$H_\varphi \cong (H_A)_\varphi + (H_F)_\varphi = -j\frac{\omega}{\eta}[A_\theta + \eta F_\varphi] \tag{2.70}$$

Using the Eqs. (2.61-2.62), the equations above can be reduced as:

$$E_r \cong 0 \tag{2.71}$$

$$E_\theta \cong -\frac{j\beta e^{-j\beta r}}{4\pi r}(L_\varphi + \eta N_\theta) \tag{2.72}$$

$$E_\varphi \cong +\frac{j\beta e^{-j\beta r}}{4\pi r}\left(L_\theta - \eta N_\varphi\right) \tag{2.73}$$

$$H_r \cong 0 \tag{2.74}$$

$$H_\theta \cong +\frac{j\beta e^{-j\beta r}}{4\pi r}\left(N_\varphi - \frac{L_\theta}{\eta}\right) \tag{2.75}$$

$$H_\varphi \cong -\frac{j\beta e^{-j\beta r}}{4\pi r}\left(N_\theta + \frac{L_\varphi}{\eta}\right) \tag{2.76}$$

In the rectangular coordinate system, the Eqs. (2.63-2.64) can be expressed as:

$$\mathrm{N} = \iint_S \mathrm{J}_s e^{j\beta r' cos\varphi} ds' = \iint_S (\hat{a}_x J_x + \hat{a}_y J_y + \hat{a}_z J_z) e^{j\beta r' cos\varphi} ds' \tag{2.77}$$

$$\mathrm{L} = \iint_S \mathrm{M}_s e^{j\beta r' cos\varphi} ds' = \iint_S (\hat{a}_x M_x + \hat{a}_y M_y + \hat{a}_z M_z) e^{j\beta r' cos\varphi} ds' \tag{2.78}$$

Using the Cartesian-to-spherical components transformation, the equations above can be reduced to:

$$\mathrm{N}_\theta = \iint_S (J_x cos\theta cos\varphi + J_y cos\theta sin\varphi - J_z sin\theta) e^{+j\beta r' cos\psi}\, ds' \tag{2.79}$$

$$\mathrm{N}_\varphi = \iint_S (-J_x sin\varphi + J_y cos\varphi) e^{+j\beta r' cos\psi}\, ds' \tag{2.81}$$

$$L_\theta = \iint_S (M_x cos\theta cos\varphi + M_y cos\theta sin\varphi - M_z sin\theta) e^{+j\beta r' cos\psi}\, ds' \quad (2.82)$$

$$L_\varphi = \iint_S (-M_x sin\varphi + M_y cos\varphi) e^{+j\beta r' cos\psi}\, ds' \quad (2.83)$$

In summary, the procedure of calculating radiation characteristics is given by the following steps [20]:

1. Select a close surface over which the actual current density $\boldsymbol{J}_s$ or the equivalent current densities $\boldsymbol{J}_s$ and $\boldsymbol{M}_s$ exists.

2. Specify the current density $\boldsymbol{J}_s$ and $\boldsymbol{M}_s$ using Huygen's principle:

$$\boldsymbol{J}_s = \hat{n} \times \boldsymbol{H}_a \quad (2.84)$$

$$\boldsymbol{M}_s = -\hat{n} \times \boldsymbol{E}_a \quad (2.85)$$

where $\hat{n}$ represents the unit vector normal to the surface S, $\boldsymbol{H}_a$ represents the total magnetic field over the surface S, and $\boldsymbol{E}_a$ represents the total electric field over the surface S.

3. Determine N_θ, N_φ, L_θ, and L_φ using Eqs. (2.79-2.83).

4. Determine the far-field $\boldsymbol{E}$ and $\boldsymbol{H}$ fields using Eqs. (2.71-2.76).

This procedure is applied in calculating the Radiation Pattern for the antenna models in FUNSAFE.

Fresnel-Fraunhofer Boundary Sphere

The fields around an antenna can be divided into two principle regions: *Fresnel zone* and *Fraunhofer zone*. The *Fresnel zone* represents the region near the antenna which is also called the *near field*, while the *Fraunhofer zone* is the region at a large distance from the antenna that is

usually called the *far field*. As shown in references [28, 29], the interface between *near field* and *far field*, which is also called the *Fresnel-Fraunhofer boundary sphere*, can be represented as:

$$R = 2D^2/\lambda \tag{2.86}$$

where D is the maximum dimension of the antenna, and λ is the wavelength. However, this distance is not applicable for all situations, and it mainly works for electrically large antennas. The derivation of this distance will be discussed below [3, 30].

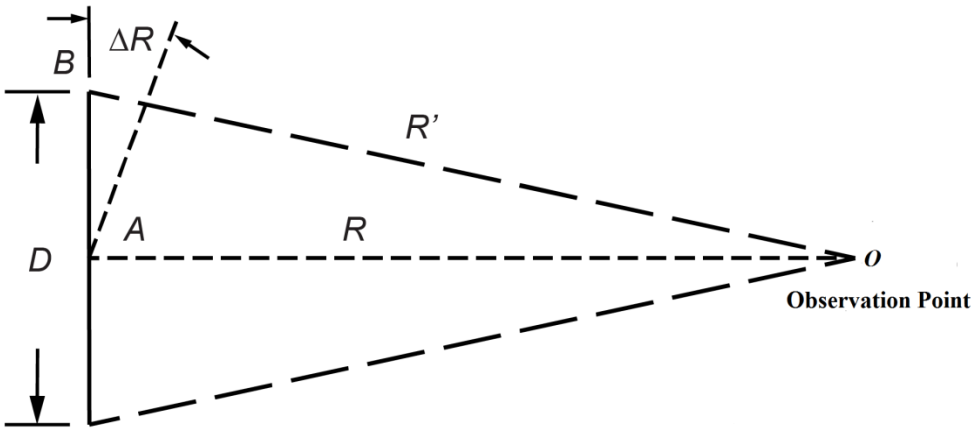

Figure 2 Derivation of Fresnel-Fraunhofer Boundary Sphere

As shown in Fig. 2, *D* represents maximum dimension of the antenna, and *R* represents the distance between the observation point *O* and the antenna to be investigated. Then the difference in path length between the outer edge of *D* and the center is given by

$$\Delta R = R' - R \tag{2.87}$$

Appling the Pythagorean Theorem to the triangle OAB, the following equation is obtained:

$$R^2 + (D/2)^2 = (R + \Delta R)^2 \tag{2.88}$$

Supposing that $(\Delta R)^2$ is negligible, then the equation above is reduced to:

$$R = \frac{D^2}{8\Delta R} \tag{2.89}$$

If the path difference is set to $\Delta R = \lambda/16$, then we have:

$$R = \frac{2D^2}{\lambda} \tag{2.90}$$

which is a safe distance to use if the maximum phase deviation of $\pi/8$ is not too large for the antenna [30].

However, for the monopole model discussed in Chapter III, the largest dimension of the antenna D is equal to $\lambda/4$, which can be easily seen from the name quarter-wavelength monopole. In this case, a maximum phase deviation of $\pi/8$ is obviously too large for the antenna, since the maximum phase deviation along the whole antenna is only $\pi/2$. Hence, the commonly used Fresnel-Fraunhofer boundary cannot be applied for the quarter-wavelength monopole antenna, and the real boundary between near field and far field should be larger than this distance.

CHAPTER III

MONOPOLE ANTENNA

Introduction

Characteristics and Applications

The monopole antenna is one of the simplest quarter-wavelength narrowband antennas, which is a popular test case for electromagnetic simulations. In 1990, James G Maloney proposed accurate computation of the radiation for simple antennas using FDTD [31], a cylindrical monopole antenna was discussed there. Later, some kinds of antennas developed from monopole antennas were discussed with FDTD method [32, 33]. In Makarov's book [34], the monopole antenna is a basic test case for verification of the MoM methods discussed in the book. In Jin's book [10], the monopole antenna is an important example of narrowband antennas for verification of the finite element methods. Monopole antennas are widely used in communication systems, and their applications include broadcasting, car radios, and cellular telephones.

As a typical model of narrowband antennas, monopole antennas have a relatively large percent bandwidth of approximately 10%. The monopole antenna is fed by a coaxial cable and does not require a balun transformer to realize impedance matching. A thin monopole antenna is a numerically challenging example since a fine surface mesh of the entire monopole length is necessary in order to get accurate results [34].

Working Theory

Relationship to Balanced Antennas

The monopole antenna is a derivative form of the dipole antenna which was used in the first wireless electromagnetic system demonstrated by Professor Heinrich Rudolph Hertz [2].

Suppose that a monopole is mounted on an ideally infinite ground plane, according to image theorem, its impedance and radiation characteristics can be deduced from that of a dipole of twice its length in free space. For a base-driven monopole, its input impedance is equal to one-half that of the center-driven dipole, and the radiation pattern above the infinite ground plane is identical with the upper half of the radiation pattern of the corresponding dipole [28].

Effect of Finite-Size Ground Plane on Impedance and Pattern

Practically, because the ideal infinite ground plane does not exist in the real world, measurements are made on a test site with a finite size. Several methods were developed to investigate the characteristics of a monopole antenna on a finite-size ground plane. Bolljahn first considered the problem from the point of view of symmetrical components [35]. His original work was developed by assuming a short monopole on a disk. Later, Storer extended Bolljahn's study to monopoles of arbitrary length [36].

According to Storer, the difference of the input impedance from a finite-size ground plane to an infinite-size ground plane of a base-driven monopole erected upon a large circular ground plane can be written as

$$\Delta Z = Z - Z_0 = j\frac{60}{kd}e^{-jkd}\left|k\int_0^h \frac{I(z)}{I(0)}dz\right|^2 \tag{3.1}$$

where Z_0 represents impedance of monopole referred to an infinite ground plane in Ω, d represents diameter of circular ground plane, h is the height of the monopole, $I(z)$ represents current-distribution function of monopole, and $I(0)$ represents base current or input current. k in the equation represents the wave number which can be expressed as:

$$k = 2\pi/\lambda \tag{3.2}$$

For a quarter-wavelength monopole, if we assume $I(z) = I(0)\cos kz$, then

$$\left| k \int_0^h \frac{I(z)}{I(0)} dz \right| = 1 \tag{3.3}$$

Thus, the difference of resistance dR and the reactance dX of a quarter-wavelength monopole from the finite-size ground plane antenna to the infinite-size ground plane antenna are shown in Fig. 3. As the size of the ground plane becomes larger, the difference becomes more and more insignificant, and the result will become closer to that of the infinite ground plane.

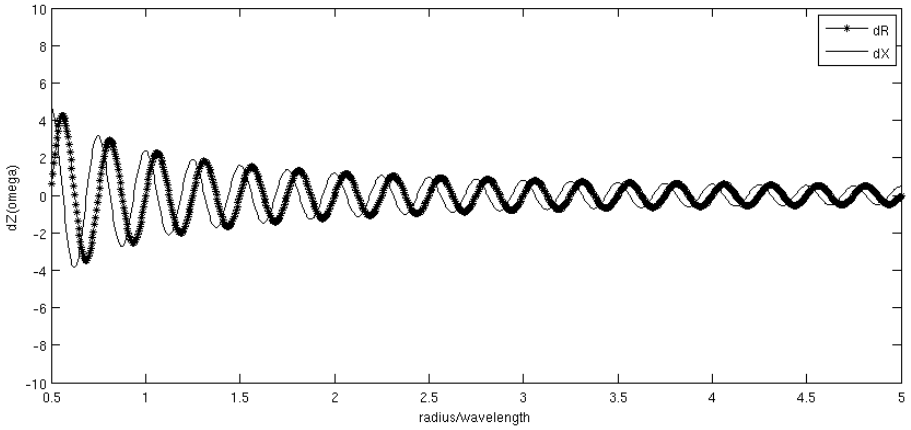

Figure 3 Difference of Impedance between Finite-Size and Infinite-Size Ground Plane Monopole Antenna over the Ratio of Radius to Wavelength

Although the size of the ground plane has small effects on the values of input impedance at the resonant frequency, the resonant frequency should be the same for different cases.

Consequently, the effect of the size of the ground plane on S_{11} is insignificant. However, the radiation pattern is affected by the size of the ground plane considerably. Analytically, uniform geometrical theory of diffraction(GTD) [37] is applied in obtaining the accurate pattern of monopole on finite-size ground plane.

Later in this Chapter, the effect of ground plane size on the antenna characteristics will be discussed according to simulation results obtained by FUNSAFE and HFSS.

Antenna Model and Field Distribution

The geometry of the monopole antenna is shown in Fig. 4, and the details of parameters are discussed below. r_{in} and r_{out} are the radius of inner conductor and outer conductor of the coaxial cable, respectively. *R* represents the radius of ground plane which is also the radius of the hemispherical computational domain. *h=50mm* is the height of the monopole, which is $\lambda/4$ for quarter-wavelength monopole antenna. ε_r is the relative permittivity of the material in the coaxial cable, which is set to 2.2 in the monopole antenna case.

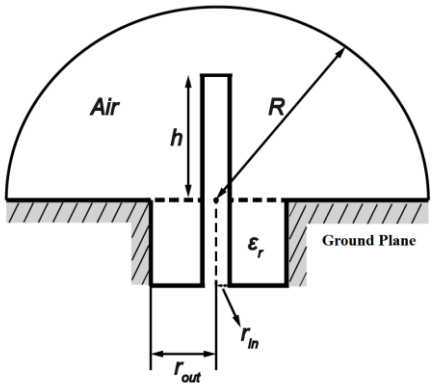

Figure 4 Geometry of Monopole Antenna

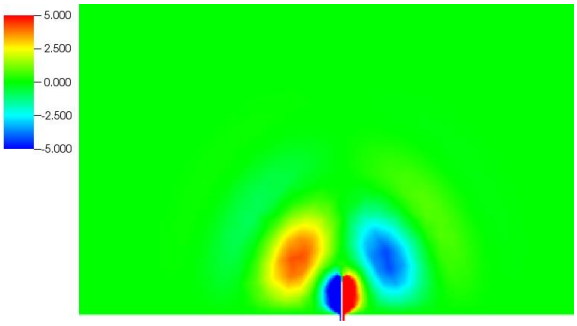

(a) Ex on x-z plane at time t1=0.625

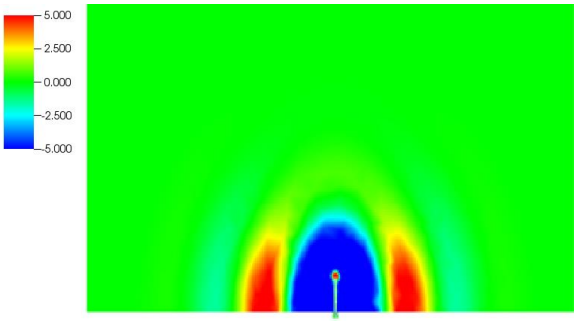

(b) Ez on x-z plane at time t1=0.625

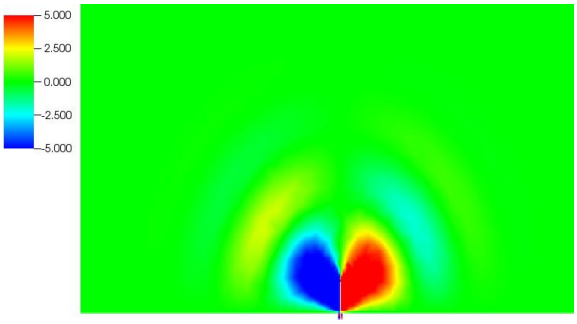

(c) Ex on x-z plane at time t_2=0.700

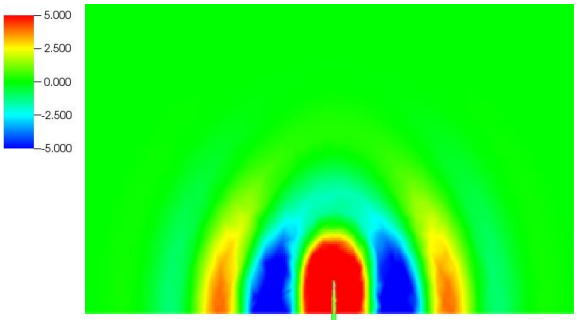

(d) Ez on x-z plane at time t_2=0.700

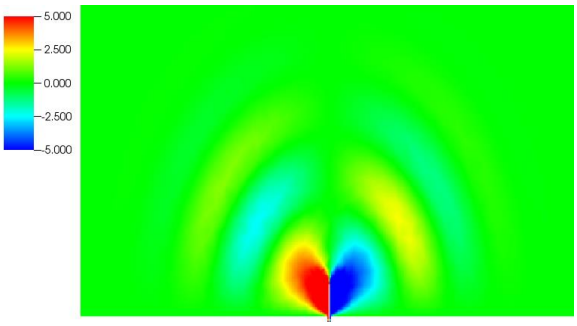

(e) Ex on x-z plane at time t_3=0.800

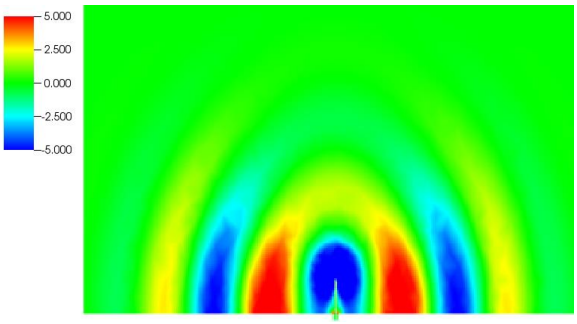

(f) Ez on x-z plane at time t_3=0.800

Figure 5 Electric Fields of Monopole Antenna on x-z Plane

The electric field is plotted on x-z plane at the selected time steps where the Gaussian pulse is large enough for observation of fields. As shown in Fig. 5, the electric field of the monopole antenna transmits periodically from the center of the ground plane to

the outer space.

Effect of Ground Plane Size on Antenna Characteristics

In this section, the monopole antenna shown in Fig. 4 is simulated in three cases with $R = 60\text{mm}(0.3\lambda)$, $R = 200\text{mm}(\lambda)$ and $R = 600\text{mm}(3\lambda)$, respectively. The simulation results of S_{11} and Radiation Pattern obtained by both FUNSAFE and HFSS are discussed below.

In this thesis, antenna cases are run with HFSS for comparison. In HFSS, the outer boundary condition is selected with the option of *radiation boundary*, while in FUNSAFE, PML or Silver-Muller boundary condition is applied. The *radiation boundary* in HFSS is introduced to truncate the infinite space into one confined simulation space, and it is similar to the Silver-Muller boundary condition applied in FUNSAFE. In HFSS, a series of adapted meshes are generated for each run [14], and the refined level of the mesh is determined by the *Maximum Delta S* (the maximum change in the magnitude of the scattering parameters between two consecutive passes). For the antenna cases considered in this thesis, the *Maximum Delta S* in HFSS is set to be a reasonable level that maximizes the solution convergence level within the current computer resource. However, it should be noted that the solution obtained by HFSS may not represent a fully converged solution. Moreover, due to the use of adaptive mesh refinement in HFSS, the final mesh used for the test cases discussed later is considerably smaller than the mesh used in FUNSAFE.

Effect of Ground Plane Size on S_{11}

Theoretically, the ideal resonant frequency for quarter-wavelength monopole antenna with $D = 50mm(\lambda = 200mm)$ should be 1.5GHz [25, 28]. In practice, due to the effects of the ground plane and the coaxial feeding line, the resonant frequency will have a small shift from the theoretical results. In testing the simulation results of S_{11} for monopole antennas with different ground sizes, both PML and the Silver-Muller boundary condition are applied. The results in three simulation methods are compared: FUNSAFE with PML, FUNSAFE with the Silver-Muller boundary condition and HFSS with radiation boundary.

In the first case, the radius of the ground plane is 60mm(0.3λ), and this means the radius of hemispherical computational domain for the monopole antenna also has the same value. Since the Silver-Muller boundary condition is applicable in the region where the wave is traveling normal to the boundary, the distance of 0.3λ is not far enough to meet the requirement of the Silver-Muller boundary condition. As shown in Fig. 6, the value of S_{11}(dB) of the antenna with PML is lower than that of the antenna with Silver-Muller boundary condition, which means in the PML case the antenna has lower reflection on the resonant frequency than in the Silver-Muller case. Also, since radiation boundary is applied in HFSS, the result of S_{11} in HFSS simulation is closer to the one in FUNSAFE with Silver-Muller boundary condition. In conclusion, the hemispherical computational domain of $R = 60\text{mm}(0.3\lambda)$ is not sufficient enough to get accurate results when using a radiation boundary condition that assumes the outgoing waves are normal to the boundary.

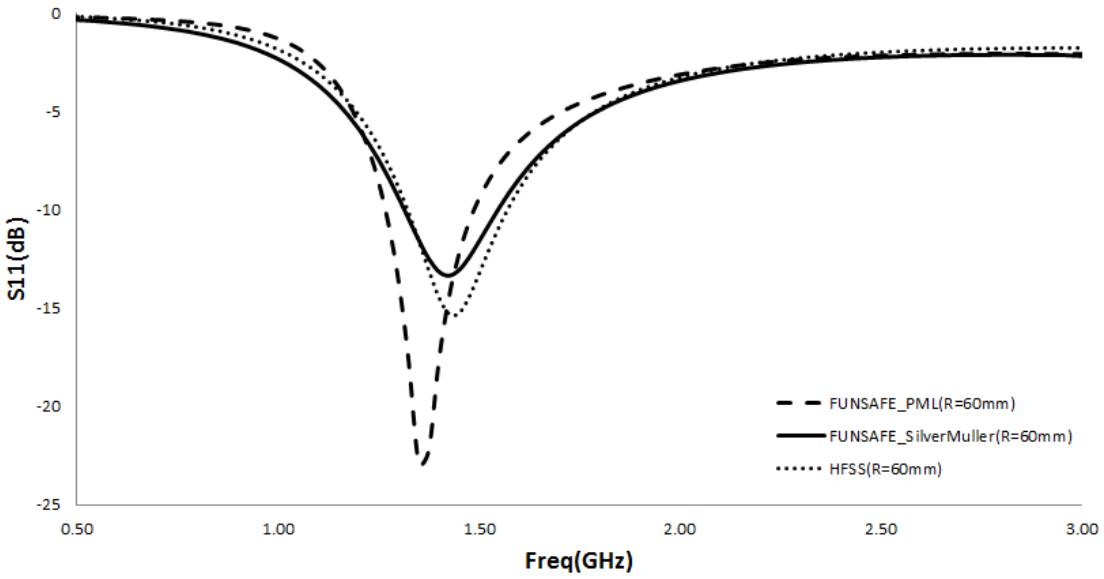

Figure 6 Comparison of S_{11} with FUNSAFE on Medium Mesh with the P2 Scheme and HFSS in the Case of Monopole Antenna (R=60mm(0.3λ))

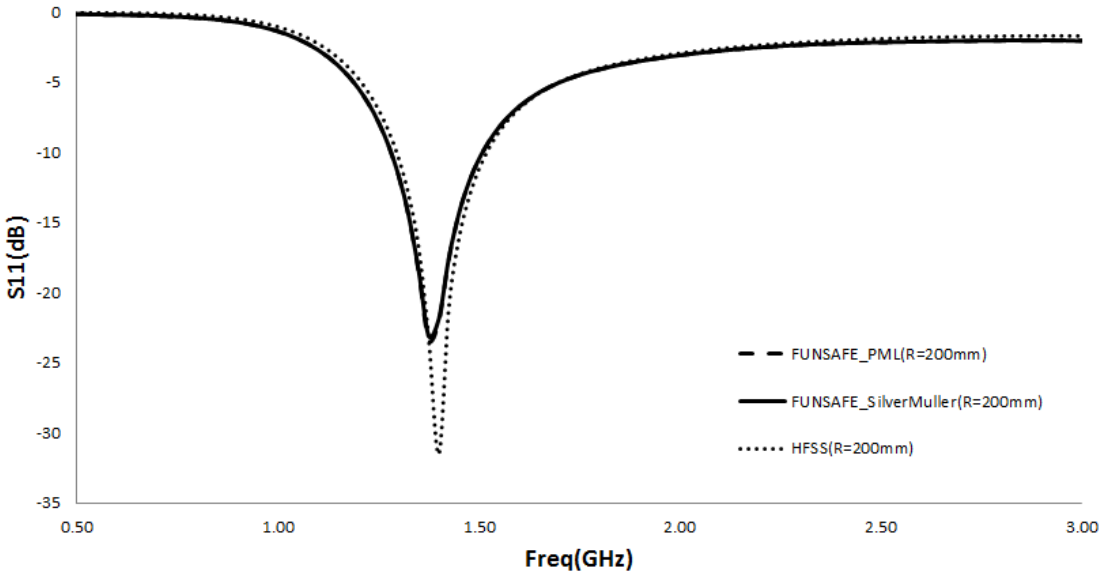

Figure 7 Comparison of S_{11} with FUNSAFE on Medium Mesh with the P2 Scheme and HFSS in the Case of Monopole Antenna (R=200mm(λ))

In the second and third case, the radius of the ground plane is 200mm(λ) and 600mm(3λ), respectively, which are also the radius of hemispherical computational domain for the monopole antenna. The distance is far enough to meet the requirement of the Silver-Muller boundary condition. As shown in Fig. 7 and Fig. 8, the resonant frequency of S_{11} in three cases match each other well when $R \gg \lambda$. Since the results of S_{11} in FUNSAFE with PML and Silver-Muller boundary condition have few differences with each other, they are hard to distinguish in Fig. 7 and Fig. 8.

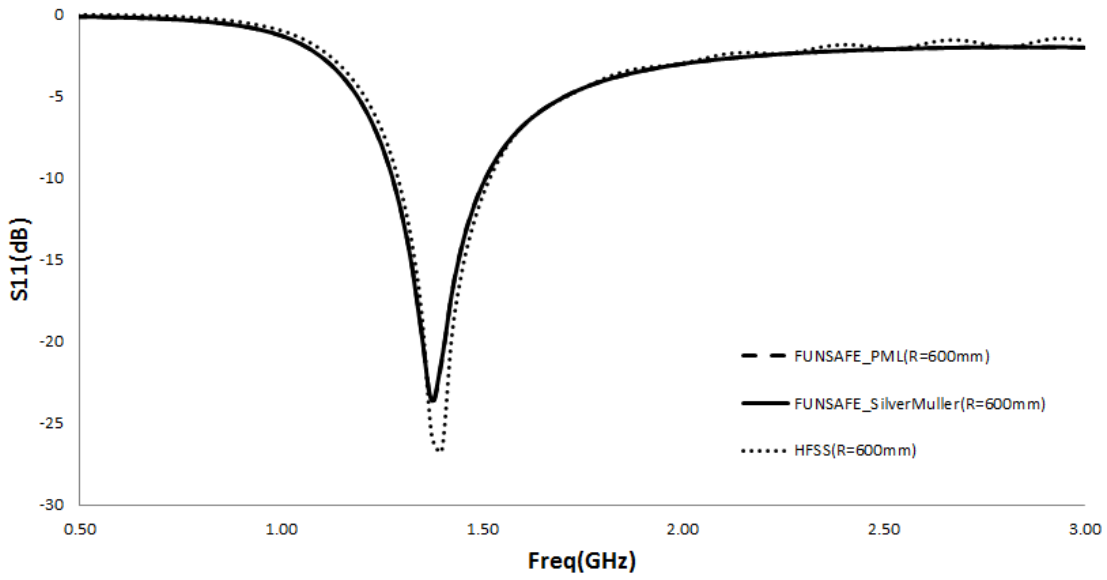

Figure 8 Comparison of S_{11} with FUNSAFE on Medium Mesh with the P2 Scheme and HFSS in the Case of Monopole Antenna (R=600mm(3λ))

In summary, the dimensions of the radius of ground plane have little effect on the resonant frequency of S_{11} for the quarter-wavelength monopole antenna, which can be shown clearly in Fig. 9. In the current simulation model, the dimensions of the hemispherical computational domain are limited by the size of the ground plane, and they will lead to

inaccuracy of the computational results for the antenna case with a relatively small ground plane when a radiation boundary condition that assumes the outgoing waves are normal to the boundary is applied.

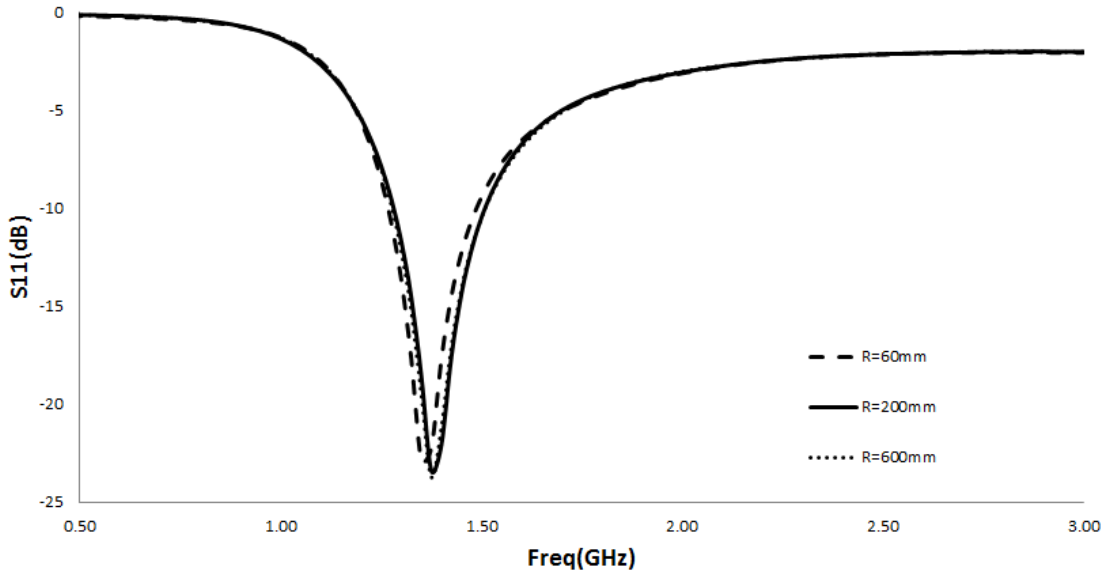

Figure 9 Comparison of S_{11} with Different Sizes of Ground Plane by FUNSAFE with PML on Medium Mesh with the P2 Scheme in the Case of Monopole Antenna

Effect of Ground Plane Size on Radiation Pattern

Opposite to the little effect on S_{11}, the dimensions of the radius of ground plane have much effect on the radiation pattern. The ground plane in a monopole antenna acts as a reflector, and its dimension determines how much wave will be reflected above the plane.

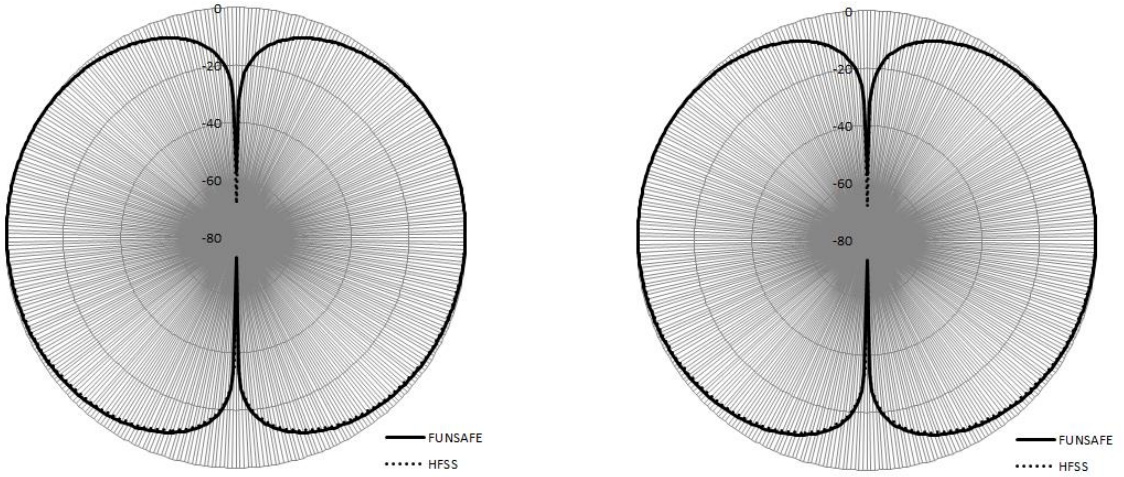

(a) E-plane (b) H-plane

Figure 10 Comparison of Radiation Pattern at 1.35GHz with FUNSAFE on Medium Mesh with the P2 Scheme and HFSS in the Case of Monopole Antenna (R=60mm(0.3λ))

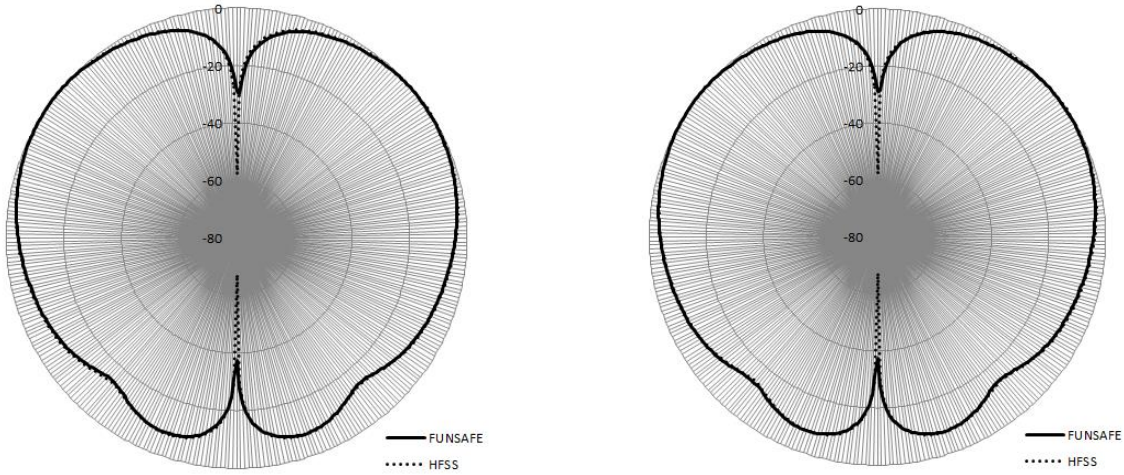

(a) E-plane (b) H-plane

Figure 11 Comparison of Radiation Pattern at 1.35GHz with FUNSAFE on Medium Mesh with the P2 Scheme and HFSS in the Case of Monopole Antenna (R=200mm(λ))

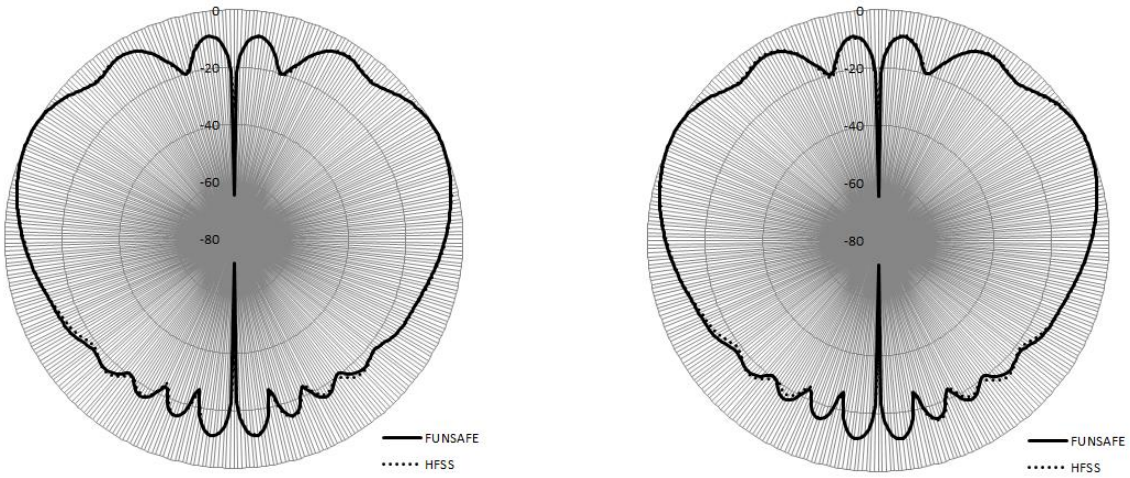

(a) E-plane (b) H-plane

Figure 12 Comparison of Radiation Pattern at 1.35GHz with FUNSAFE on Medium Mesh with the P2 Scheme and HFSS in the Case of Monopole Antenna (R=600mm(3λ))

The E-plane($\varphi = 0$) and H-plane($\varphi = \pi/2$) normalized radiation pattern of antennas with ground plane of $R = 60\text{mm}(0.3\lambda)$, $R = 200\text{mm}(\lambda)$ and $R = 600\text{mm}(3\lambda)$ are shown in Figs. 10, 11, and 12, respectively. The results of HFSS and FUNSAFE match well. As the ground size becomes larger, the side beam becomes smaller. The effect of ground plane on Radiation Pattern is also indicated in [38]. Since the monopole antenna is an omnidirectional antenna, the radiation patterns for E-plane and H-plane are almost the same.

Grid Convergence Performance and Effect of Time-Step Sizes

Grid Convergence Behavior

To investigate the convergence behavior, the simulation code was run on four grids of different mesh sizes. The numbers of tetrahedrons and nodes are listed for each mesh in Table 1.

For the medium and fine meshes, both p1 and p2 schemes are used. However, only the p1 scheme is applied on the realfine and veryfine meshes.

Table 1 Number of Tetrahedrons and Nodes for Different Meshes in the Case of Monopole Antenna

	medium	Fine	realfine	veryfine
Number of tetrahedrons	238377	468178	683920	2399530
Number of nodes	43839	84924	124504	454174

Grid Convergence of S_{11}

The simulation results of S_{11} for the following six cases are shown in Fig. 13: the p1 scheme applied on the medium mesh, the fine mesh, the realfine mesh and the veryfine mesh, and the p2 scheme applied on the medium mesh and the fine mesh. For the p1 cases, as the mesh becomes finer, the value of S_{11}(dB) at the resonant frequency becomes more negative. Although the veryfine mesh has 454174 points, which is about ten times the number of points in the medium mesh, the results on this mesh with the p1-order scheme still do not reach the convergence level of the medium mesh with the p2 scheme. The p2 scheme is clearly significantly more accurate than the p1 scheme when the numbers of degrees of freedom are approximately equal.

It should be noticed that, since linear geometry is applied in the mesh, the order of accuracy for the p2 scheme is about 2, while if quadratic geometry is applied, the order will increase to 3. However, while the use of a linear representation of the geometry decreases the formal order of accuracy, the p2 scheme has significantly lower error levels than the p1 scheme [15].

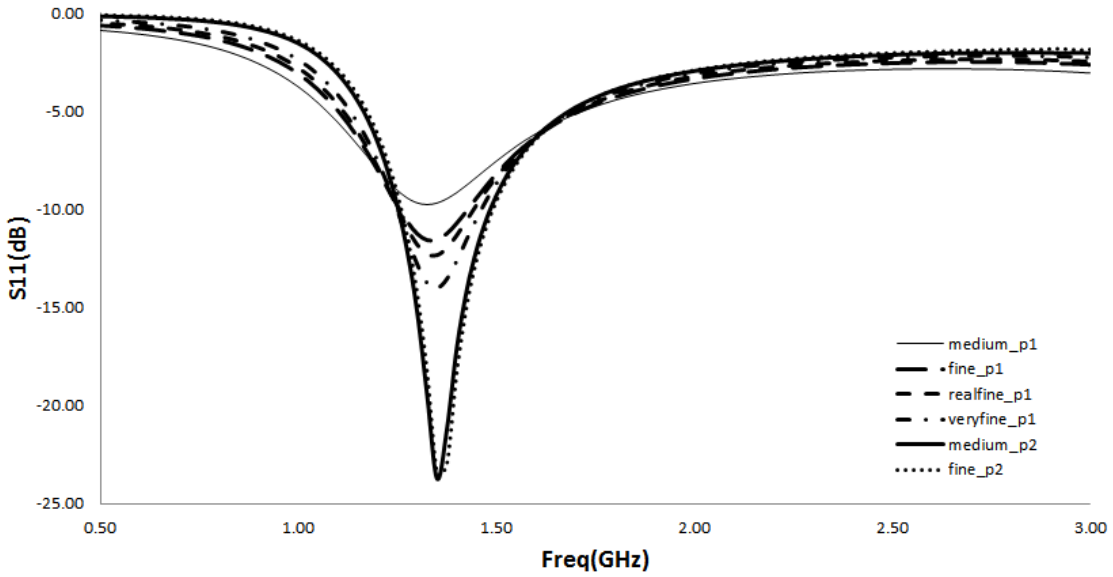

Figure 13 Comparison of S_{11} on Different Meshes with P1 and P2 Schemes in the Case of Monopole Antenna (R=600mm(3λ))

Grid Convergence of Radiation Pattern

Since the monopole antenna is an omnidirectional antenna, the radiation patterns of E-place and H-place have little difference with each other. The E-place radiation patterns for different cases are compared here. Fig. 14(a) shows the radiation patterns of the following cases: medium mesh with p1, medium mesh with p2, fine mesh with p1, fine mesh with p2. The results of p2 are more accurate than those of p1. To observe the differences more clearly, the radiation patterns are also plotted in rectangular coordinates, as shown in Fig.14(b). As the mesh becomes finer, the results of the radiation pattern tend to converge to the same value.

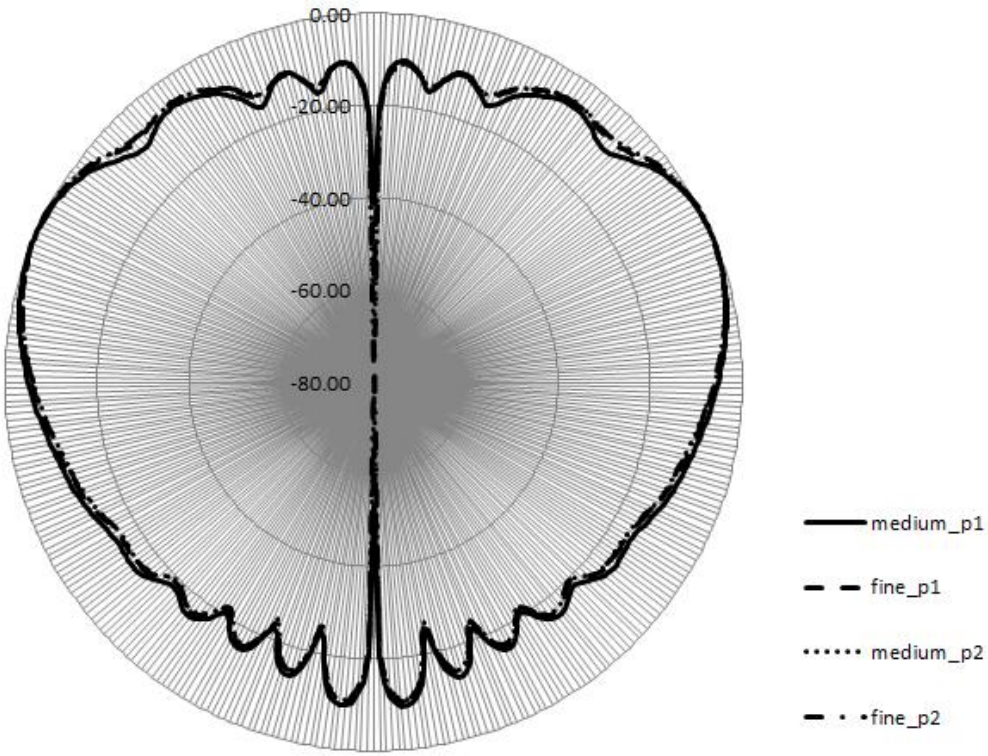

(a) Radiation Pattern in polar coordinate

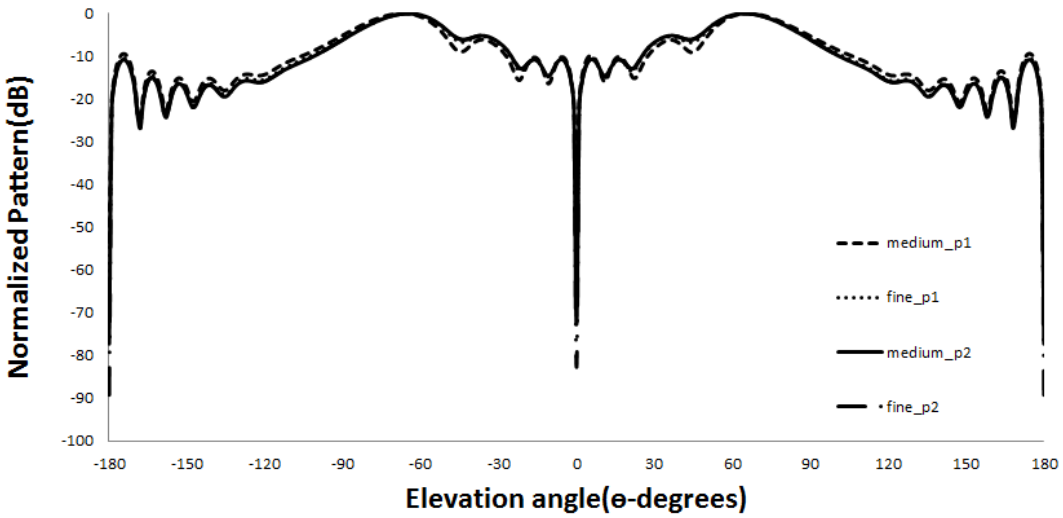

(b) Radiation Pattern in Rectangular coordinate

Figure 14 Comparison of Radiation Pattern(E-plane) at 1.35GHz on Different Meshes with P1 and P2 Schemes in the Case of Monopole Antenna (R=600mm(3λ))

Effect of Time-Step Sizes on Convergence

To investigate the effect of time-step sizes on the convergence behavior of characteristics of the monopole antenna, four cases are performed on the medium mesh with the third-order scheme: dt= dt_0, dt= 0.5*dt_0, dt= 0.25*dt_0, and dt= 2*dt_0, where dt_0=0.005. Note that this time step is non-dimensional but corresponds to a physical time step of 16.67 ps.

As shown in Fig. 15, the results of S_{11} present converged solutions for dt= dt_0, dt= 0.5*dt_0 and dt= 0.25*dt_0, and the result for dt= 2*dt_0 shows small variations with the others. This indicates the selected dt_0 is proper to solve the problem, neither too high nor too low. Using a higher time-step size degrade the accuracy of the results though it will save computational time, while using lower time-step sizes will not enhance the accuracy since the simulations already reach the convergence level.

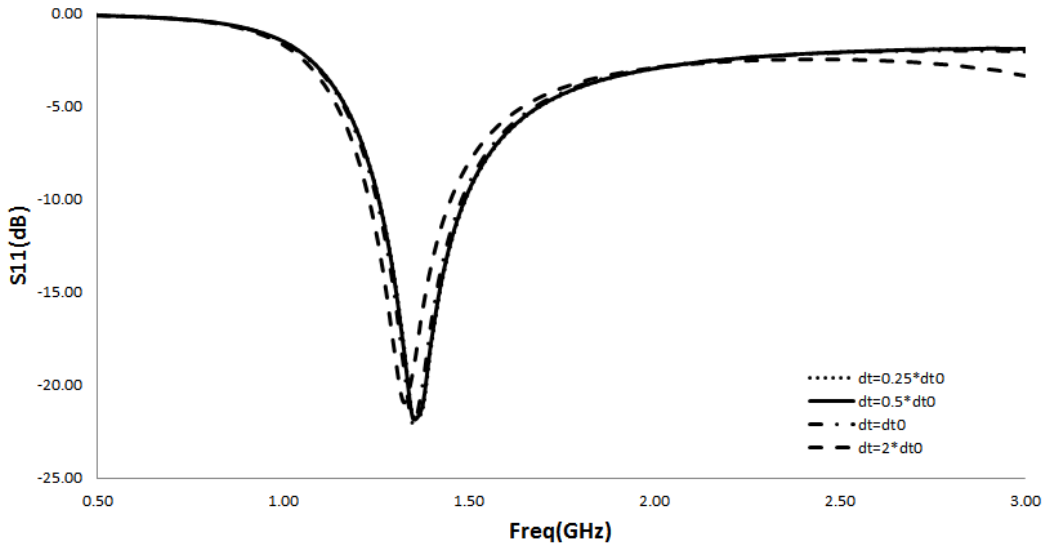

Figure 15 Comparison of S_{11} with Different Time-Step Sizes on Medium Mesh with the P2 Scheme in the Case of Monopole Antenna (R=600mm(3λ))

The requirement of the time-step size is less sensitive for the radiation pattern, as shown in Fig. 16, and the results for four different time steps match each other well. However, to ensure the accuracy of S_{11}, dt_0 is selected for the monopole case.

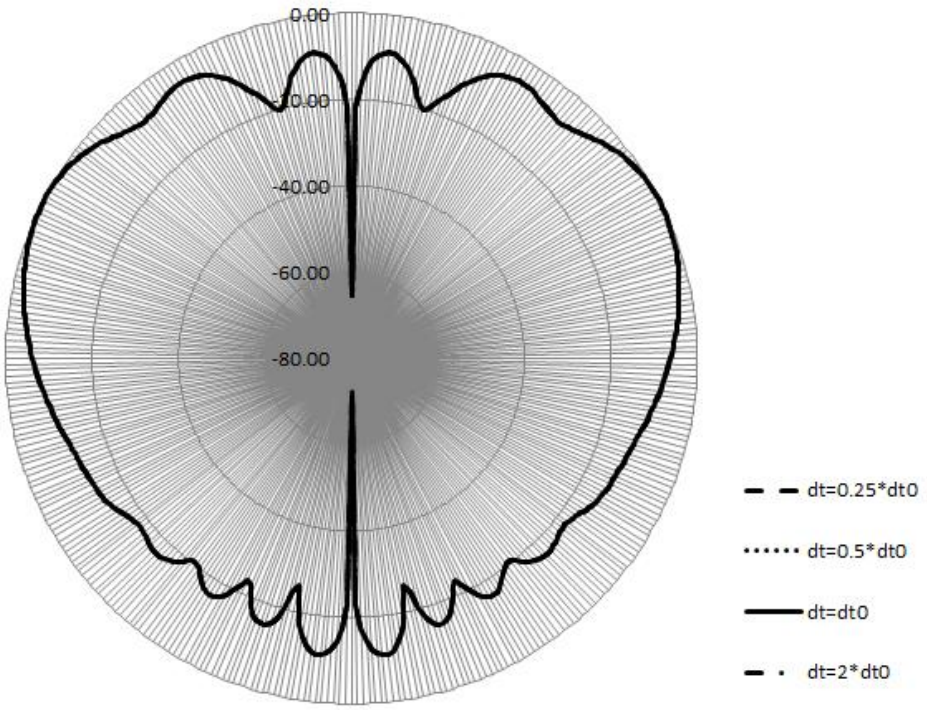

Figure 16 Comparison of Radiation Pattern (E-plane) at 1.35GHz with Different Time-Step Sizes on Medium Mesh with the P2 Scheme in the Case of Monopole Antenna (R=600mm(3λ))

Input Impedance

In this section, the convergence behavior of input impedance and the procedure of calculation will be discussed.

Grid Convergence of Input Impedance

The input impedance was calculated on both medium and fine mesh with p2 elements. The results are compared with those obtained by HFSS for verification. For a more clearly view, input admittance are plotted instead of input impedance. As shown in Fig. 17, as the mesh becomes finer, the results of input admittance agree better with the HFSS results.

Derived from Eq. (2.36), the S_{11} of the antenna can be calculated from the input impedance by:

$$S11(dB) = 20log_{10}\left|\frac{Z_{in}-Z_0}{Z_{in}+Z_0}\right| \tag{3.4}$$

where Z_{in} represents the input impedance of the antenna and Z_0 is the characteristic impedance of the coaxial cable which can be calculated by [28]:

$$Z_0 = \frac{138}{\sqrt{\varepsilon_r}} log_{10}(\frac{r_{out}}{r_{in}}) \tag{3.5}$$

The result of S_{11} calculated through input impedance is compared with the result calculated through power by Eq. (2.37). As shown in Fig. 18, the results from the two methods match well. However, for the cases that the characteristic impedance is not easy to obtain, the calculation through impedance will not work well. Also, the value of Z_0 introduced in calculating S_{11} is obtained by analytical method instead of computational method, which will lead to inaccuracy of the results.

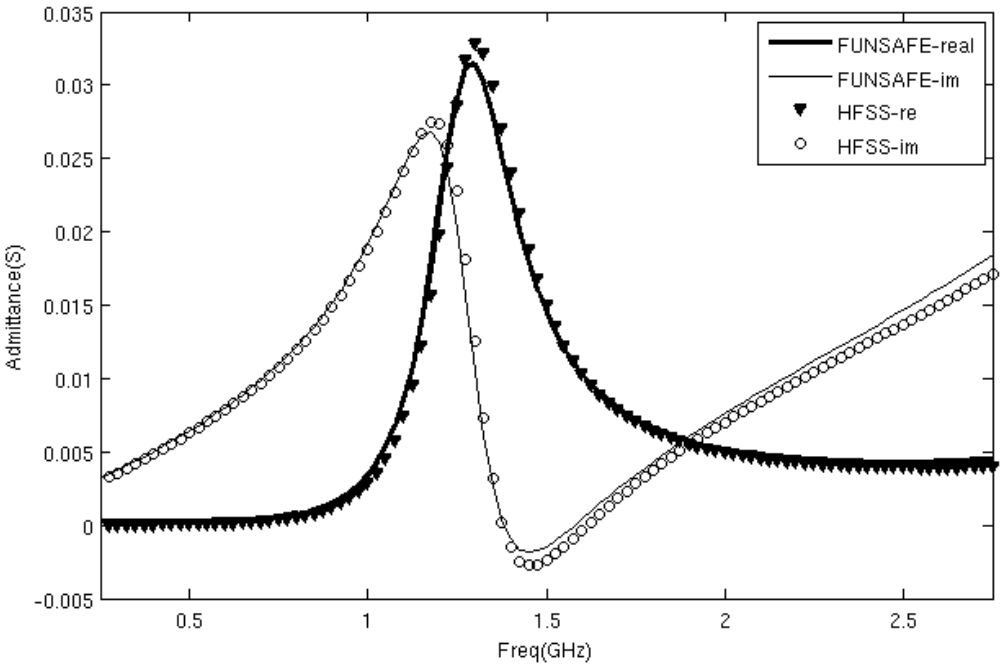

(a) Medium Mesh

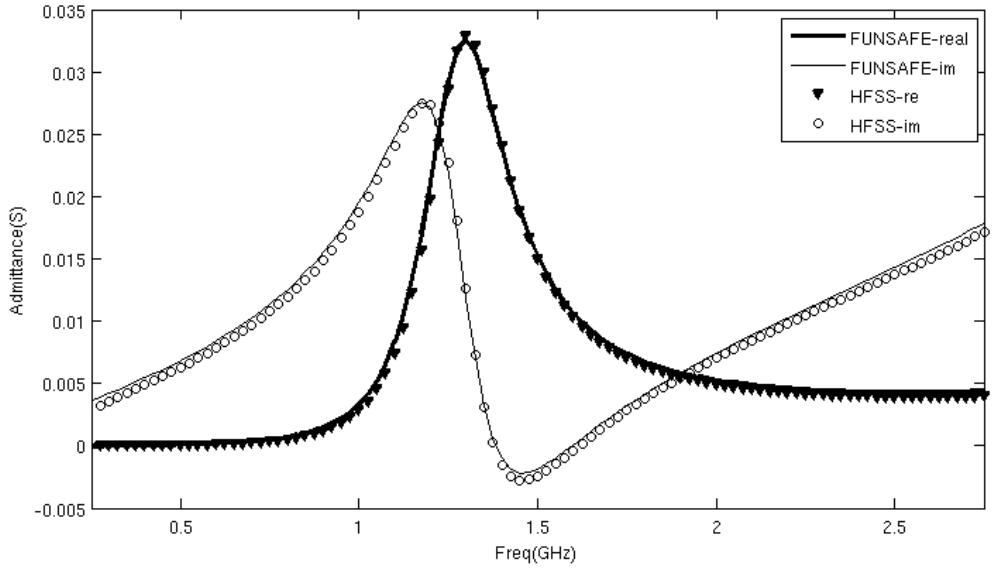

(b) Fine Mesh

Figure 17 Comparison of Input Impedance between FUNSAFE on Medium and Fine meshes with the P2 Scheme and HFSS in the Case of Monopole Antenna (R=600mm(3λ))

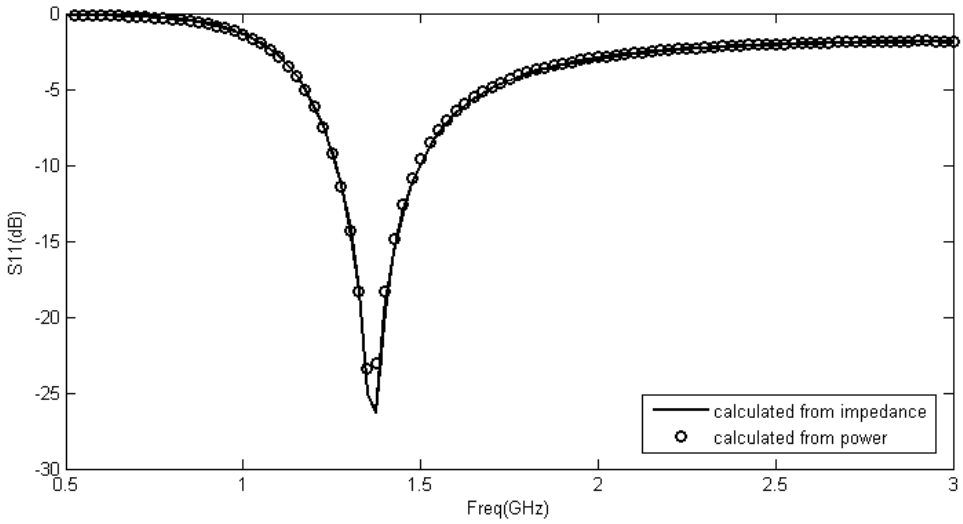

Figure 18 Comparison of S_{11} Calculated through Impedance and Power on the Fine Mesh in the Case of Monopole Antenna (R=600mm(3λ))

Procedure of Calculating the Input Impedance

As indicated earlier, the input impedance represents the ratio of voltage to current at the port. The most intuitive method to calculate the impedance is to calculate voltage and current, respectively, and then compute the ratio.

In an arbitrary two-conductor TEM transmission line, the voltage of the positive conductor relative to the negative conductor can be represented as the integral of the electric field [39]:

$$\mathrm{V} = \int_{+}^{-} \bar{E} \cdot d\bar{l} \tag{3.6}$$

where the integration path begins on the + conductor and ends on the – conductor. It should be noticed that, the voltage defined in Eq. (3.6) is unique and is independent of the integration path.

Also, the total current flowing on the + conductor can be expressed as the integration of magnetic field:

$$I = \oint_{C^+} \bar{H} \cdot d\bar{l} \tag{3.7}$$

where the integration contour can be any closed path enclosing the + conductor. That means the results should be the same no matter which closed path is chosen to integrate the current.

Since only TEM waves can be transmitted in the coaxial line, Eqs. (3.6-3.7) can be applied in calculating the voltage and current on the coaxial port. For the coaxial cable, according the working theory of coaxial transmission line, the inner conductor is related to the positive conductor and the outer conductor is related to the nagative conductor. From the ideas above, the procedure for calculating input impedance for the coaxial-line feed monopole antenna simulated on parallel systems is developed:

1. Select all the points on the face of the coaxial port and save the relevant information of coordinates, E-field and H-field in independent arrays for each processor.
2. Collect the information above from each process to one process.
3. Transfer the coordinates from rectangular coordinate system to spherical coordinate system.
4. Select points with r coordinates in a relatively small range, then sort the selected points by the value of θ, and these points will form a closed path. The sum of the dot product of the vector between two adjacent points and the average of $\vec{H}$ of two adjacent points along the whole close path will be the current.

$$I = \sum_{i=1}^{n-1} \frac{\vec{H}_i + \vec{H}_{i+1}}{2} \cdot \vec{n}_{i,i+1} + \frac{\vec{H}_n + \vec{H}_1}{2} \cdot \vec{n}_{n,1} \tag{3.8}$$

5. Select points with θ coordinates in a relatively small range, then sort the selected points by the value of r, and these points will form a path from the inner conductor to the outer one. The sum of the dot product of the vector between two adjacent points and the average of $\vec{E}$ of two adjacent points along the whole path will be the voltage.

$$\mathrm{V} = \sum_{i=1}^{n-1} \frac{\vec{E}_i + \vec{E}_{i+1}}{2} \cdot \vec{n}_{i,i+1} \tag{3.9}$$

where point of $\mathrm{i} = 1$ represents the point on the inner conductor, while point of $\mathrm{i} = \mathrm{n}$ represents the point on the outer conductor. The result is the voltage of the inner conductor relative to the outer conductor.

6. Then the input impedance or input admittance can be calculated:

$$\mathrm{Z} = \frac{V}{I} \tag{3.10}$$

$$\mathrm{Y} = \frac{I}{V} \tag{3.11}$$

where the input impedance and input admittance are relevant to the total electric field and total magnetic field obtained at the coaxial port.

It should be noticed that, the $\vec{E}$ and $\vec{H}$ discussed above represent Fourier Transformed values and are therefore in complex format. As a result, the relevant V and I are also in complex format, and then the input impedance or input admittance is in complex format.

To verify the ideas above, current and voltage are calculated by selecting different paths. For current calculations, five different paths are selected: r=(2.0mm,2.1mm), r=(2.3mm,2.4mm), r=(2.5mm,2.6mm), r=(2.7mm,2.8mm), and r=(3.0mm,3.1mm). As shown in Fig. 19, the current calculated along different paths match each other well.

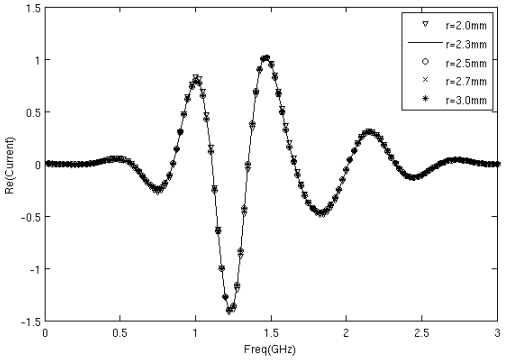

(a)Real part of current

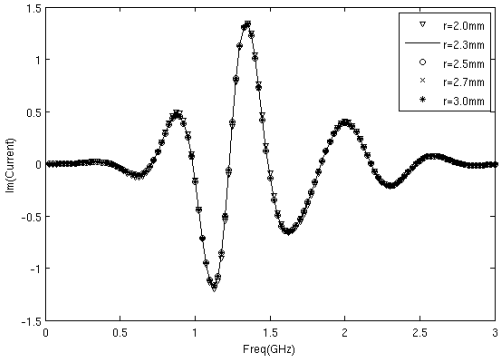

(b)Image part of current

Figure 19 Comparison of Current at the Coax Port along Different Paths for Simulations on the Fine Mesh in the Case of Monopole Antenna (R=600mm(3λ))

For calculation of voltage, four different paths are selected: $\theta = (0, \frac{\pi}{32})$, $\theta = (\frac{\pi}{2}, \frac{17\pi}{32})$, $\theta = (\pi, \frac{33\pi}{32})$, and $\theta = (\frac{3\pi}{2}, \frac{49\pi}{32})$. As shown in Fig. 20, the voltage calculated along different paths match each other well.

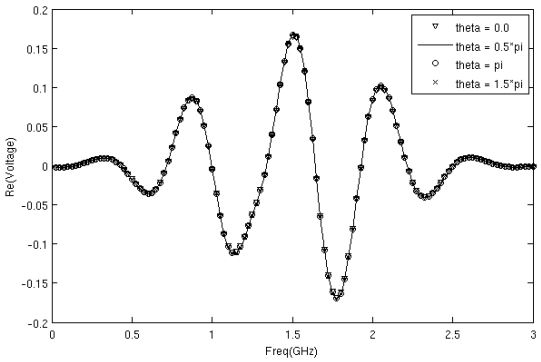

(a)Real part of voltage

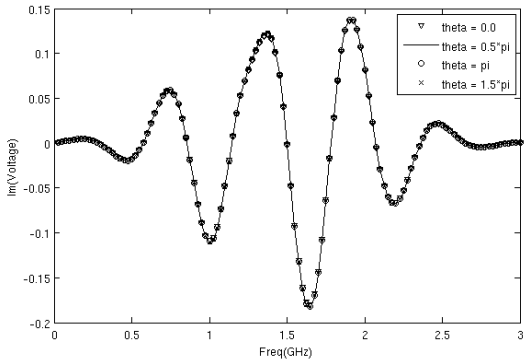

(b)Image part of voltage

Figure 20 Comparison of Voltage at the Coax Port along Different Paths for Simulations on the Fine Mesh in the Case of Monopole Antenna (R=600mm(3λ))

The procedure above is verified to be effective in calculating the input impedance for coaxial-line fed antenna, as shown in Fig. 17. However, it can only apply on coaxial-line fed models. More generally applicable methods for calculation of input impedance should be developed in future work.

CHAPTER IV

PATCH ANTENNA

Introduction

Patch antennas are typically narrowband antennas, which are commonly used in verifying the accuracy of electromagnetic simulations. Jin and Makarov applied their computational simulations on the patch antenna for verification of the finite element method and MoM [10, 34]. The patch antenna is also a test case in the HFSS tutorial [40], where the geometry and dimensions of the patch antennas discussed below come from.

Characteristics and Applications

Patch Antennas, also called microstrip antennas, are popular for applications in the microwave frequency range (300MHz-300GHz). The patch antennas are easy to manufacture, as both single-elements and element-arrays, due to their simplicity and compatibility with printed-circuit technology. They commonly consist of a patch of metal, usually rectangular or circular, on a thin layer of dielectric, which is called the substrate, on a ground plane, as shown in Fig. 21.

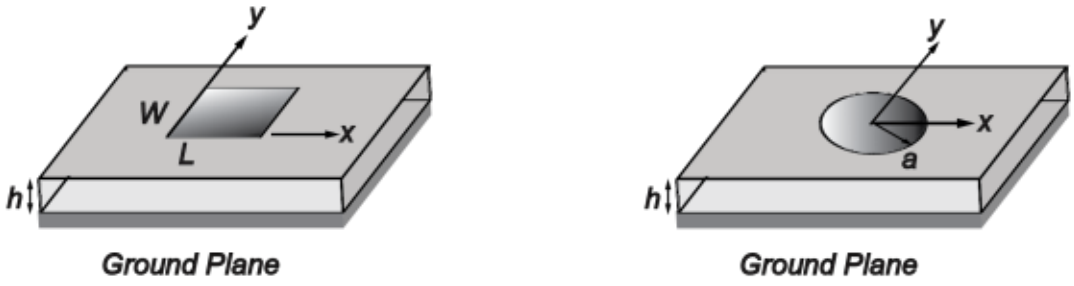

(a) rectangular patch (b)circular patch

Figure 21 Model of Microstrip Patch Antennas

Due to the characteristics of low-profile, conformability to planar and nonplanar surface, low-cost to manufacture, microstrip patch antennas are widely used in high-performance aircraft, satellite, and missile applications where low-cost, high-performance, and ease of installation are required. These antennas also have commercial applications, such as wireless communications and mobile radio.

The first microstrip patch antenna was introduced by Munson in 1972 [41]. Later, Howell introduced the circular patch according to the basic idea of Munson's paper [42]. In 1976, Dernery proposed the transmission-line model for analysis of microstrip antennas [43]. Later, the cavity model [44] and the spectral-domain method [45] were developed to analyze the characteristics of patch antennas.

Feeding Methods

The microstrip patch antennas have various feeding methods, among which the most popular ones are coaxial-line feed, microstrip-line feed, proximity-coupled feed and aperture-coupled feed [25]. The coaxial-line feed and the microstrip-line feed are introduced below.

Coaxial-line Feed

As shown in Fig. 22, when a coaxial cable is applied in feeding the patch antenna, the inner conductor of the coax is attached to the radiation patch while the outer conductor is connected to the ground plane. The coaxial probe feed is easy to fabricate and match, and it has low spurious radiation. However, the coaxial-line feed will limit the bandwidth for the designs with thick substrates. This feeding method is applied in simulations of the patch antennas in this thesis.

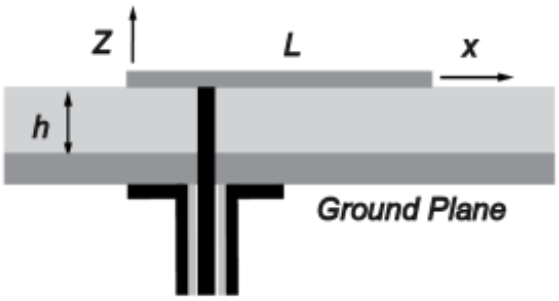

Figure 22 Coaxial-line Feed Model

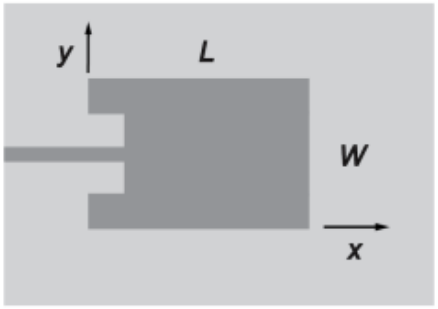

Figure 23 Microstrip-line Feed Model

Microstrip-line Feed

The microstrip-line feed is shown in Fig. 23. It is simple to match by controlling the inset position and also simple to model. However, this feeding method will lead to an increase of surface waves and spurious feed radiation for the models with higher thickness of substrate [25]. The microstrip-line feed is commonly used in antenna arrays while the coaxial-line feed works better for stand-alone elements. This model will be developed in future work.

Working Theory

There are various analysis methods for microstrip patch antennas, among which the most popular ones are the transmission-line model, cavity model and full wave model [25]. The transmission-line model is the easiest but less accurate. The cavity model is more accurate but more complex compared to the transmission-line model. The details of cavity model are discussed below.

Fringing Effects

Before introducing the cavity model, the fringing effects need to be explained first. The fields at the edges of the patch undergo fringing because of the finite dimensions of the patch along length and width. The amount of fringing is a function of patch dimensions and substrate height. Since the waves travel both in substrate and air, the effective dielectric constant ε_{eff} is introduced to account for fringing and wave propagation. From reference [20], the effective dielectric constant is given by:

$$\varepsilon_{eff} = \frac{\varepsilon_r+1}{2} + \frac{\varepsilon_r-1}{2}\left[1 + 12\frac{h}{W}\right]^{-1/2} \tag{4.1}$$

where ε_r is the permittivity of the substrate, and h is the height of the substrate. The equation above applies for the cases where the length of the patch L is the resonant dimension, and then W in the equation represents the width of the patch.

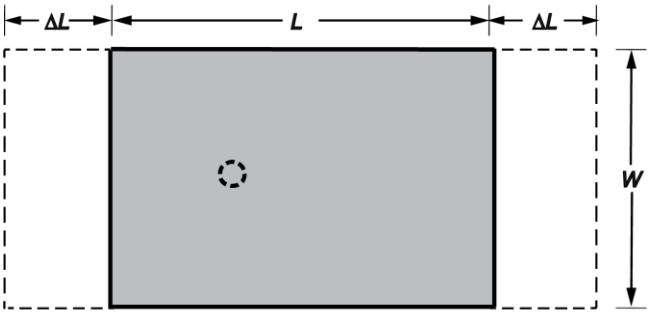

(a)top view

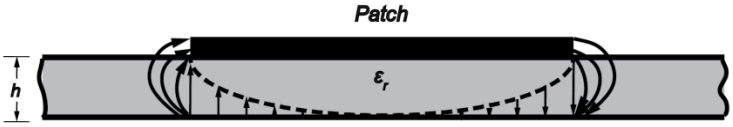

(b)side view

Figure 24 Physical and Effective Lengths of Microstrip Patch

The field along the resonant dimension L and the effective lengths caused by edge effects are shown in Fig. 24. Due to fringing, the microstrip patch looks wider electrically compared to its physical dimensions. A practical approximate relation for the normalized extension of the length is indicated in [46], given by:

$$\frac{\Delta L}{h} = \frac{0.412(\varepsilon_{eff}+0.3)(\frac{W}{h}+0.264)}{(\varepsilon_{eff}-0.258)(\frac{W}{h}+0.8)} \tag{4.2}$$

where ε_{eff} is effective dielectric constant obtained by Eq. (4.1), and h is the height of the substrate. The extension of the length ΔL is added to the resonant dimension L, while W in the equation represents the width of the patch.

Cavity Model

In the cavity model, the dielectric substrate (the part between the patch and the ground plane) of the microstrip patch antenna is treated as a cavity. This cavity has electric conductors above and below it and magnetic walls along the perimeter of the patch.

As shown in Fig. 25, the charge distribution of the cavity model is controlled by the attractive mechanism and the repulsive mechanism [47]. The attractive mechanism works between the corresponding opposite charges on the bottom side of the patch and the ground plane, and it tends to maintain the charge concentration on the bottom of the patch. The repulsive mechanism works between charges on the bottom surface of the patch, and it tends to push some charges from the bottom of the patch to its top surface around its edges.

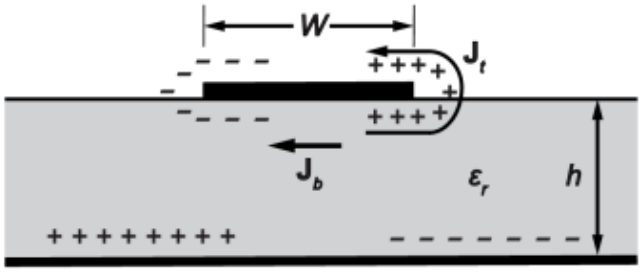

Figure 25 Current Distribution of Cavity Model

In practice, the height-to-width ratio of the patch is very small, the current flow around the edges of the patch will be small, and then the tangential magnetic fields at the edges will be very small. Since the height of the substrate is very small ($h \ll \lambda$), the field variations along the height will be negligible. In addition, the fringing of the fields along the edges of the patch are also very small. And then the electric field is nearly normal to the surface of the patch, therefore only TM^z field configurations will be considered within the cavity. From the discussions above, for the cavity model, the top and bottom walls are perfectly electric conducting, and the four side walls will be modeled as perfectly magnetic walls, as shown in Fig. 26.

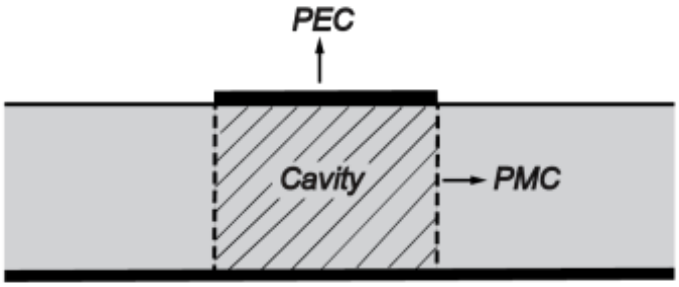

Figure 26 Boundary Conditions of Cavity Model

The electric and magnetic fields within the cavity are related to the vector potential A_x given by [20]:

$$E_x = -j\frac{1}{\omega\mu\varepsilon}\frac{\partial^2 A_z}{\partial x \partial z} \tag{4.3}$$

$$E_y = -j\frac{1}{\omega\mu\varepsilon}\frac{\partial^2 A_z}{\partial y \partial z} \tag{4.4}$$

$$E_z = -j\frac{1}{\omega\mu\varepsilon}\left(\frac{\partial^2}{\partial z^2} + k^2\right)A_z \tag{4.5}$$

$$H_x = \frac{1}{\mu}\frac{\partial A_z}{\partial y} \tag{4.6}$$

$$H_y = -\frac{1}{\mu}\frac{\partial A_z}{\partial x} \tag{4.7}$$

$$H_z = 0 \tag{4.8}$$

where

$$A_z = [A_1 \cos(k_x x) + B_1 \sin(k_x x)]\,[A_2 \cos(k_y y) + B_2 \sin(k_y y)]\,[A_3 \cos(k_z z) + B_3 \sin(k_z z)] \tag{4.9}$$

and subject to the boundary conditions of

$$E_y(0 < x' \leq L, 0 < y' \leq W, z' = 0) = 0 \tag{4.10}$$

$$E_y(0 < x' \leq L, 0 < y' \leq W, z' = h) = 0 \tag{4.11}$$

$$H_y(x' = 0, 0 < y' \leq W, 0 < z' \leq h) = 0 \tag{4.12}$$

$$H_y(x' = L, 0 < y' \leq W, 0 < z' \leq h) = 0 \tag{4.13}$$

$$H_x(0 < x' \leq L, y' = 0, 0 < z' \leq h) = 0 \tag{4.14}$$

$$H_x(0 < x' \leq L, y' = W, 0 < z' \leq h) = 0 \tag{4.15}$$

Applying the boundary conditions in Eq. (4.9), the final form of the vector potential A_z is:

$$A_z = A_{mnp}\cos(k_x x')\cos(k_y y')\cos(k_z z') \tag{4.16}$$

where A_{mnp} represents the amplitude coefficients of each *mnp* mode. The wave numbers k_x, k_y, k_z are given by:

$$k_x = \frac{m\pi}{L} \tag{4.17}$$

$$k_y = \frac{n\pi}{W} \tag{4.18}$$

$$k_z = \frac{p\pi}{h} \tag{4.19}$$

where m, n and p represent the number of half-cycle field variations along the x, y and z directions, respectively. Since the wave numbers k_x, k_y, k_z are subject to the constraint equation:

$$k_x^2 + k_y^2 + k_z^2 = (\frac{m\pi}{L})^2 + (\frac{n\pi}{W})^2 + (\frac{p\pi}{h})^2 = \omega_r^2 \mu\varepsilon \quad (4.20)$$

then the resonant frequencies for the cavity are given by:

$$(f_r)_{mnp} = \frac{1}{2\pi\sqrt{\mu\varepsilon}} \sqrt{(\frac{m\pi}{L})^2 + (\frac{n\pi}{W})^2 + (\frac{p\pi}{h})^2} \quad (4.21)$$

The mode with the lowest resonant frequency is referred to as the dominant mode. From the equations above not only dominant mode but also higher order modes can be derived. The dominant mode and higher order modes are determined by the relationships among the dimensions of the antenna.

If $L > W > h$, the dominant mode is the TM_{100}^z, and the resonant frequency is given by:

$$(f_r)_{100} = \frac{c}{2L\sqrt{\varepsilon_r}} \quad (4.22)$$

where *c* is the speed of light in free space. In this case, if $L > W > \frac{L}{2} > h$, the second order mode is the TM_{010}^z, and the resonant frequency is given by:

$$(f_r)_{010} = \frac{c}{2W\sqrt{\varepsilon_r}} \quad (4.23)$$

But if $L > \frac{L}{2} > W > h$, the second order mode is the TM_{200}^z, and the resonant frequency is given by:

$$(f_r)_{200} = \frac{c}{L\sqrt{\varepsilon_r}} \quad (4.24)$$

If $W > L > h$, the dominant mode is the TM_{010}^z, and the resonant frequency is given by:

$$(f_r)_{010} = \frac{c}{2W\sqrt{\varepsilon_r}} \quad (4.25)$$

In this case, if $W > L > \frac{W}{2} > h$, the second order mode is the TM_{100}^z, and the resonant frequency is given by:

$$(f_r)_{100} = \frac{c}{2L\sqrt{\varepsilon_r}} \quad (4.26)$$

But if $W > \frac{W}{2} > L > h$, the second order mode is the TM_{020}^{z}, and the resonant frequency is given by:

$$(f_r)_{020} = \frac{c}{W\sqrt{\varepsilon_r}} \tag{4.27}$$

Based on the equations above, the E_z field distribution along the side walls of the cavity for the TM_{100}^{z} mode, TM_{010}^{z} mode, TM_{200}^{z} mode, and TM_{020}^{z} mode is shown in Fig. 27, respectively.

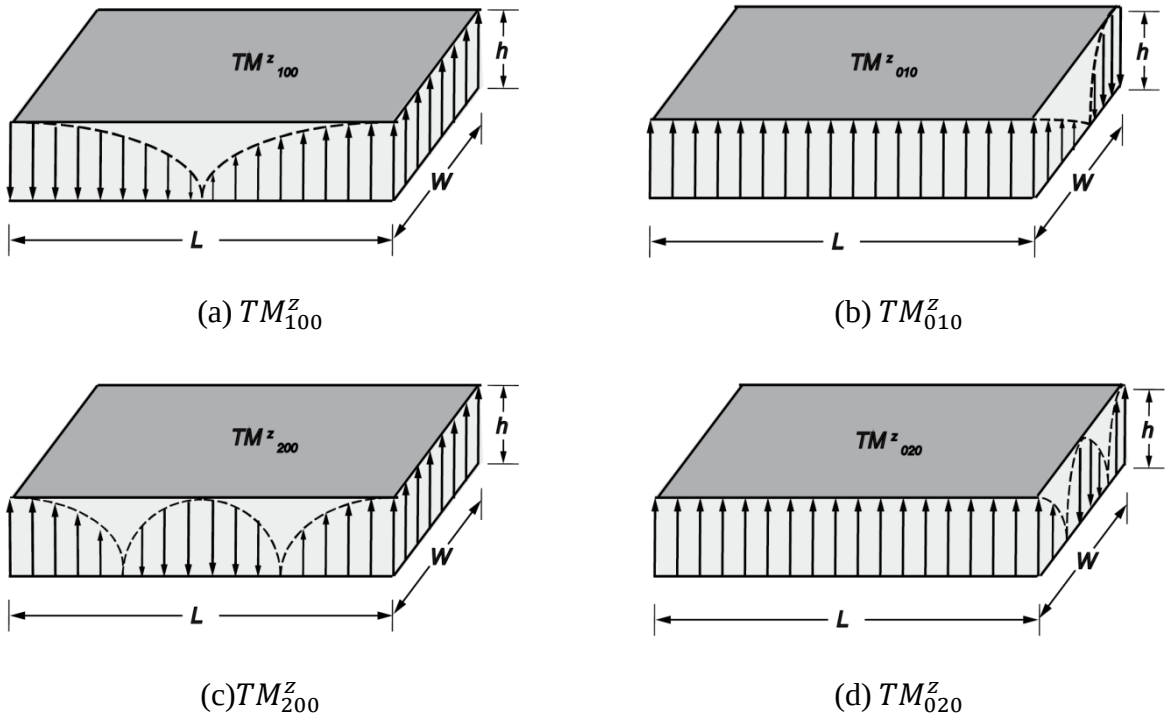

(a) TM_{100}^{z} (b) TM_{010}^{z}

(c)TM_{200}^{z} (d) TM_{020}^{z}

Figure 27 Field Modes of Cavity Model

The discussions above are based on the assumption that there is no fringing of fields along the edges of the cavity. When the effective length is taken into consideration, the modified formula of Eqs. (4.22-4.27) which includes edge effects is given by:

$$f_r = \frac{c}{2(L+2\Delta L)\sqrt{\varepsilon_r}} \tag{4.28}$$

where c is the speed of light in free space and ΔL is the fringing extension added to the resonant dimension L calculated by Eq. (4.2). L and ΔL here can be replaced by W and ΔW when W is the resonant dimension. According to the Eq. (4.28), the real frequency will be a little lower than the ideal values calculated by the Eqs. (4.22-4.27). Some examples discussed below will illustrate what the real resonant frequency looks like.

Antenna Model and Field distribution

The geometry of the patch antenna is shown in Fig. 28, and the details of the parameters are discussed below. r_{in} and r_{out} are the radius of inner conductor and outer conductor of the coaxial cable, respectively, and *x=5mm* is the shift distance between the coordinate origin and the center of the coaxial cable. *a=100mm* and *b=90mm* represent the dimensions of the substrate along x and y direction, respectively. *L=40mm* and *W=30mm* represent the dimensions of the patch along x and y direction, respectively. *h=3.2mm* is the height of the substrate, *t=0.1mm* is the height of the patch, and ε_{r1} and ε_{r2} are the relative permittivity of the material in the coaxial cable and the material of the substrate, respectively.

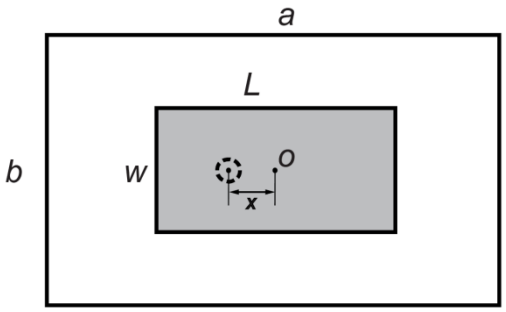

(a)top view

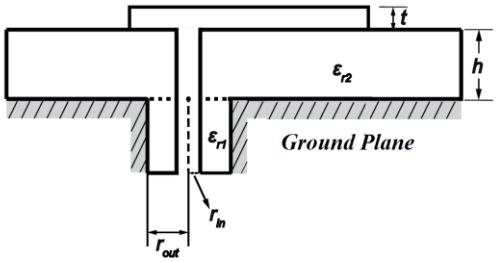

(b) cut-plane view

Figure 28 Geometry of Patch Antenna

The electric field is plotted on both the x-z plane and the patch at the selected time steps where the Gaussian pulse is large enough for observation of fields. As shown in Fig. 29, the solid line represents the side-view of the patch, and the electric field of the patch antenna transmits periodically along the patch and inside the substrate.

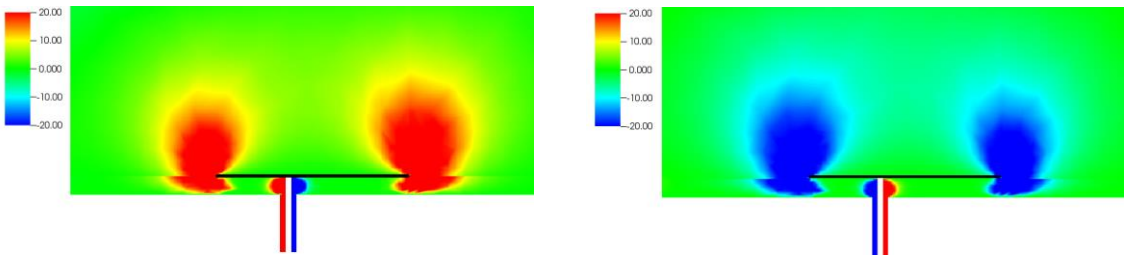

(a) Ex on x-z plane at time t_1=0.4800 (b) Ex on x-z plane at time t_2=0.5925

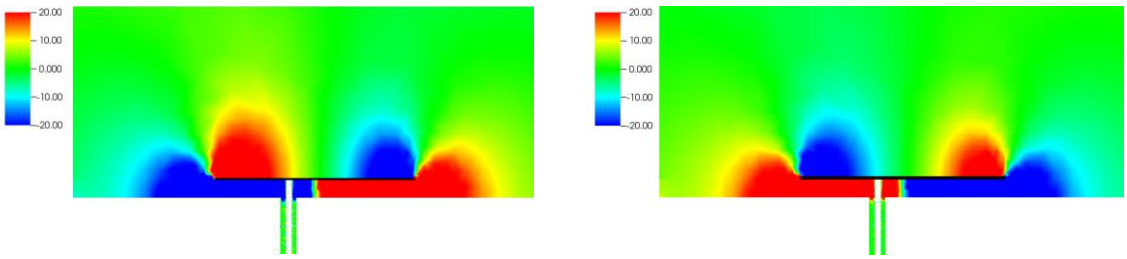

(c) Ez on x-z plane at time t1=0.4800 (d) Ez on x-z plane at time t_2=0.5925

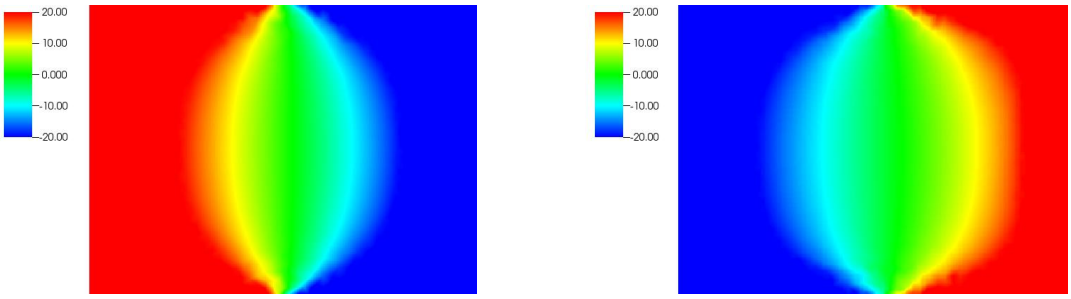

(e) Ez on the patch at time t1=0.4800 (f) Ez on the patch at time t_2=0.5925

Figure 29 Electric Fields of Patch Antenna on x-z Plane and Patch

Effect of Permittivity of Antenna Substrate on S_{11}

Theoretical Results

To investigate the effect of permittivity of antenna substrate on S_{11}, the patch antenna shown in Fig. 28 is simulated in four different cases: $\varepsilon_{r2} = 1.1$ $\varepsilon_{r2} = 2.2$ $\varepsilon_{r2} = 4.4$ and $\varepsilon_{r2} =$

6.6. To keep the characteristics of the coaxial cable the same, the permittivity of the material in the coax is set to $\varepsilon_{r1} = 2.2$ for each case. Through calculation by Eqs. (4.22-4.27), the theoretical ideal resonance frequency for each case is indicated in Table 2.

Table 2 Theoretical Ideal Resonant Frequency of Different Modes for Different Values of Relative Permittivity ε_r in the Case of Patch Antenna (GHz)

	$\varepsilon_r = 1.1$	$\varepsilon_r = 2.2$	$\varepsilon_r = 4.4$	$\varepsilon_r = 6.6$
TM^z_{100}	3.5755	2.5282	1.7877	1.4597
TM^z_{010}	4.7673	3.3710	2.3837	1.9462
TM^z_{200}	7.1510	5.0565	3.5755	2.9194
TM^z_{020}	9.5346	6.7420	4.7673	3.8925

Computational Results

The computational results of S_{11} for patch antennas with substrate material of different permittivities by FUNSAFE are shown in Fig. 30. The main and higher-order resonant frequencies for each case are list in Table 3 for convenience of comparison. Compared with theoretical results in Table 2, the differences between computational and theoretical results are discussed below.

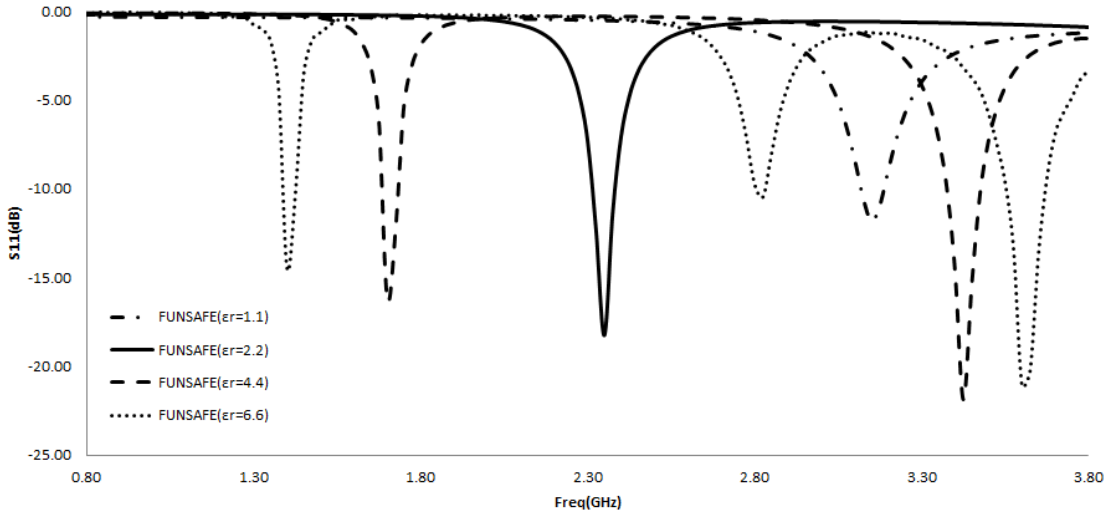

Figure 30 Comparison of S_{11} on Fine Mesh with the P2 Scheme for Different Values of Relative Permittivity ε_r in the Case of Patch Antenna

Table 3 Computational Resonant Frequency of Different Modes for Different Values of Relative Permittivity ε_r in the Case of Patch Antenna (GHz)

	$\varepsilon_r = 1.1$	$\varepsilon_r = 2.2$	$\varepsilon_r = 4.4$	$\varepsilon_r = 6.6$
1st resonant frequency	3.15	2.35	1.7	1.4
2nd resonant frequency	-	-	3.425	2.825
3rd resonant frequency	-	-	-	3.6

For the antenna with the substrate of $\varepsilon_r = 1.1$, within the frequency range from 0.8GHz to 3.8GHz, the only resonant frequency is 3.15GHz, while the theoretical resonant frequency of TM_{100}^z mode is 3.5755GHz. The difference is caused by edge effect which is not considered in the theoretical results in Table 2. As explained earlier, the edge effects will make the dimension of the patch electrically larger, which will make the resonant frequency lower than the ideal one.

For the case with the substrate of $\varepsilon_r = 2.2$, within the frequency range from 0.8GHz to 3.8GHz, the only resonant frequency is 2.35GHz, a little lower than the theoretical resonant frequency of 2.5282GHz for the TM_{100}^z mode. However, the theoretical resonant frequency of TM_{010}^z mode which is 3.3710GHz within the observed frequency range does not show up in the computational results. This phenomenon will be explained in the cases discussed below.

For the patch antenna with substrate of $\varepsilon_r = 4.4$, within the frequency range from 0.8GHz to 3.8GHz, the first and second resonant frequencies are 1.7GHz and 3.425GHz, which are close to the theoretical resonant frequencies for the TM_{100}^z mode of 1.7877GHz and the TM_{200}^z mode of 3.5755GHz. Similar to the case with $\varepsilon_r = 2.2$, the theoretical resonant frequency of 2.3837GHz for the TM_{010}^z mode does not show up in computational results.

For the case with the substrate $\varepsilon_r = 6.6$, within the frequency range from 0.8GHz to 3.8GHz, the first, second and third resonant frequencies are 1.4GHz, 2.825GHz and 3.6GHz, respectively, while the relevant theoretical resonant frequencies are 1.4597GHz, 2.9194GHz and 3.8925GHz. It should be noticed that as the permittivity increases, the equivalent wavelength in the substrate becomes smaller, and the simulation results for the same mesh will become less accurate.

From the relationship between the dimensions of the patch L and W, and according to Eqs.(4.23-4.24), the theoretical second resonant frequency for the patch antenna should be the TM_{010}^z mode. However, from the results above, the computational second resonant frequencies are closer to the theoretical results of TM_{200}^z mode than TM_{010}^z mode. The reason is that, in Eqs. (4.22-4.27), fringing effects are not taken into consideration. If considering the fringing effect,

the dimensions of the patch L and W will have new relationship in which case Eq. (4.24) will be used to calculate the second resonant frequency instead of Eq. (4.23).

Effect of Grid Quality on Convergence Behavior

Grid Optimization

As is indicated earlier, it is the fields around the edges of the patch that cause the patch antenna to radiate. This is why the mesh quality around the edges is important for accurate solutions. The following comparison of different meshes is a good proof of this point.

Table 4 Parameters for Different Meshes of Patch Antenna

	Coarse	medium	Fine
Number of tetrahedrons	107339	152671	199223
Number of points	20843	29885	38904
Number of points along L direction of the patch	40	13	40
Number of points along W direction of the patch	30	9	30

The three meshes shown in Table 4 are used to investigate the effect of mesh quality on antenna characteristics. The details about how we recognized the importance of meshes around edges will be discussed below. The first mesh generated was the medium mesh, and although the mesh initially appears to be fine enough to solve the problem, the result was not satisfactory, as shown in Fig. 31. Then the second mesh was developed which is the fine mesh with more points on the edges of the patch, and this result turns out to be reasonable. To prove the

importance of the meshes around the edges, the third mesh was generated. The third mesh is the coarse one which has about half the points of the fine mesh but the same points on the edges with the fine mesh. As shown in Fig. 31, the results of the coarse mesh and fine mesh match each other well. The investigation above is a good proof of the importance of mesh quality around the edges to obtain accurate solutions.

From the discussions above, an adaptive mesh should be a good implementation for the electromagnetic solver, which will be introduced in future work.

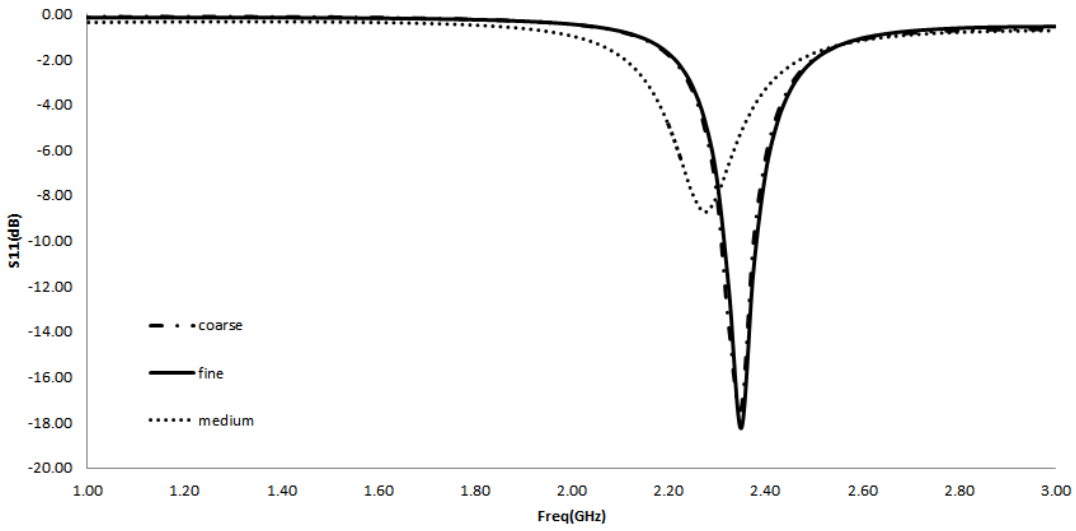

Figure 31 Comparison of S_{11} on Meshes with Different Quality with the P2 Scheme in the Case of Patch Antenna

Convergence Behavior of S_{11}

To investigate the convergence behavior of S_{11}, the FUNSAFE code was run on the coarse and fine meshes in both p1 and p2 elements, and the results are compared with those of the electromagnetic simulation software HFSS and CST.

The comparison for the case with substrate of $\varepsilon_r = 2.2$ is shown in Fig. 32. For the p1 scheme, the resonant frequency of S_{11} on the fine mesh is closer to the expected one than that on the coarse mesh, while for the p2 scheme, the difference between results on coarse and fine mesh is negligible. These differences among different simulation methods are reasonable.

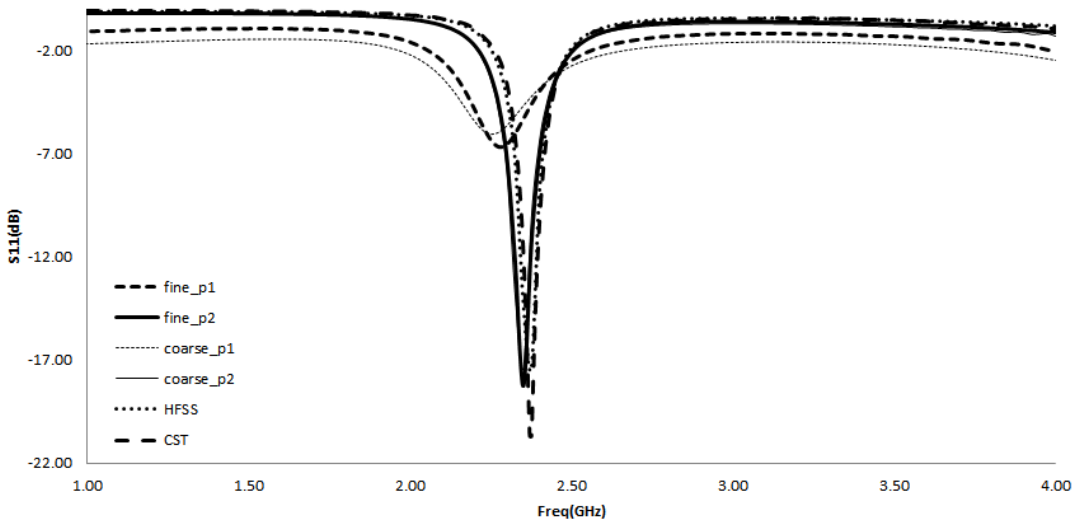

Figure 32 Comparison of S_{11} Calculated by HFSS, CST and FUNSAFE on Different Meshes with P1 and P2 Schemes in the Case of Patch Antenna ($\varepsilon_r = 2.2$)

The comparisons for the cases with substrates of $\varepsilon_r = 1.1$, $\varepsilon_r = 4.4$, and $\varepsilon_r = 6.6$ are shown in Fig. 33, 34, and 35, respectively. The resonant frequencies of the results of different simulation methods match well. The differences in values may be caused by the impedance mismatching introduced by higher permittivity of substrates. As is indicated in Chapter III, the method of calculating S_{11} in FUNSAFE is independent of impedance, while some commercial codes indeed use impedance to get the S_{11}. This is only one guess for the reason, the secret behind still needs to be explored.

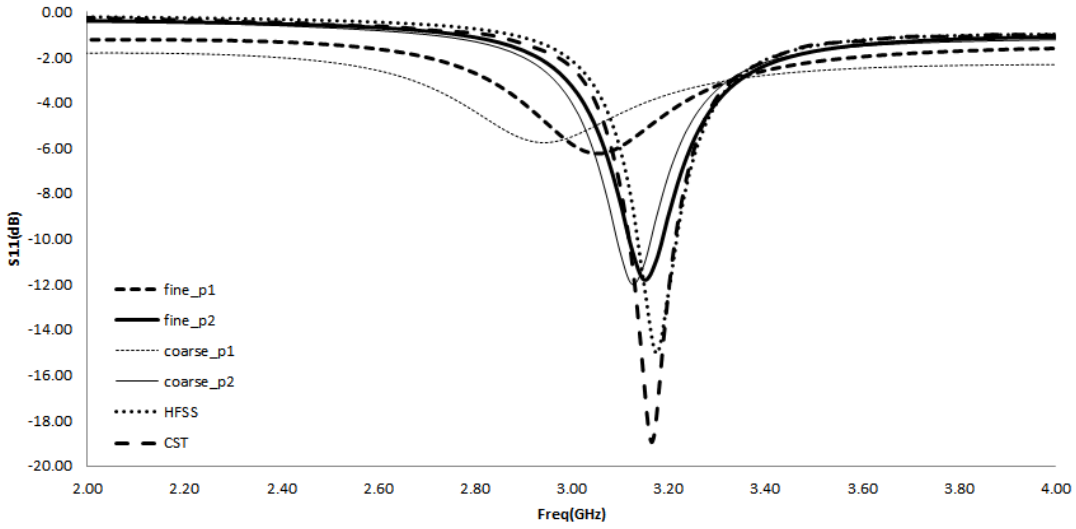

Figure 33 Comparison of S_{11} Calculated by HFSS, CST and FUNSAFE on Different Meshes with P1 and P2 Schemes in the Case of Patch Antenna ($\varepsilon_r = 1.1$)

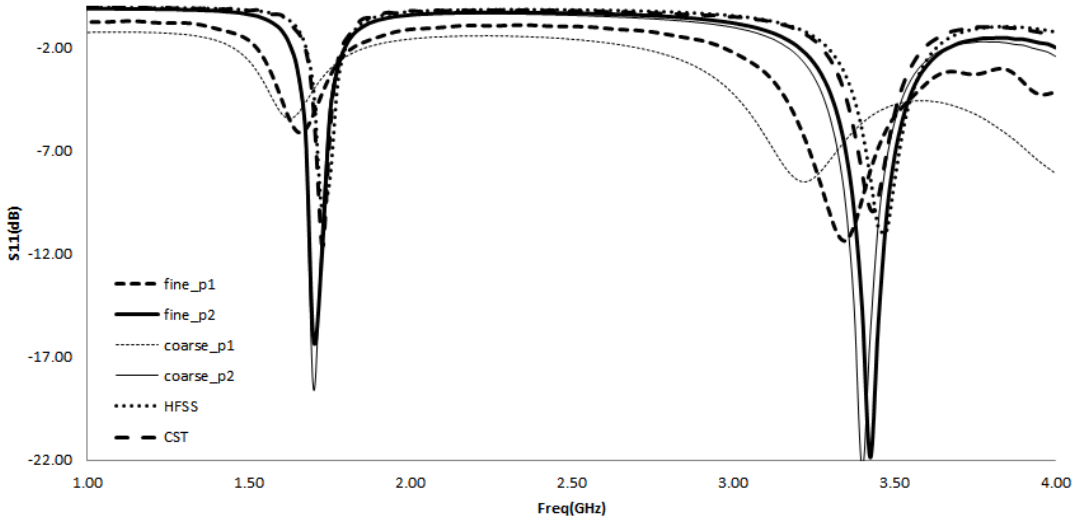

Figure 34 Comparison of S_{11} Calculated by HFSS, CST and FUNSAFE on Different Meshes with P1 and P2 Schemes in the Case of Patch Antenna ($\varepsilon_r = 4.4$)

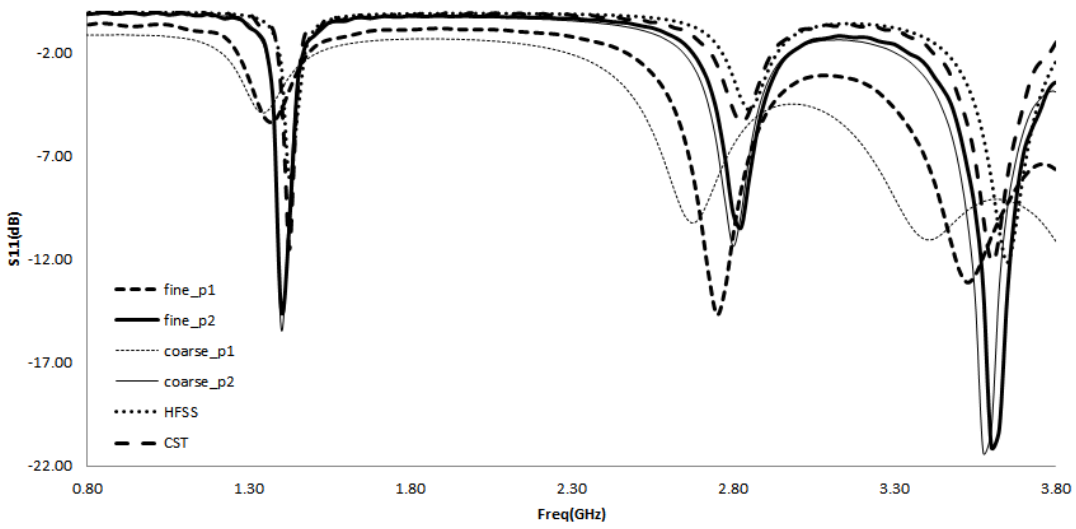

Figure 35 Comparison of S_{11} Calculated by HFSS, CST and FUNSAFE on Different Meshes with P1 and P2 Schemes in the Case of Patch Antenna ($\varepsilon_r = 6.6$)

Comparison of Radiation Pattern on Different Simulation Methods

In this section, the results of Radiation Pattern obtained by different simulation methods are compared. Since the patch antenna is not an omnidirectional antenna as the monopole antenna is, the radiation patterns for E-place and H-place are different. As shown in Fig. 36, the main lobe of the radiation pattern for each simulation result matches well, although the side lobes have some differences.

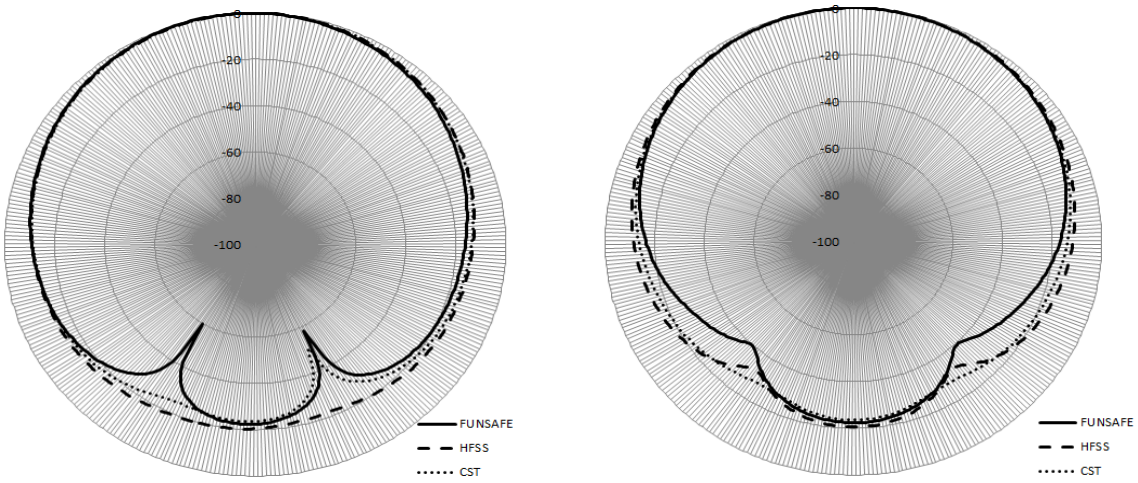

(a) E-plane(2.35GHz) (b) H-plane(2.35Hz)

Figure 36 Comparison of Radiation Pattern at 2.35GHz Calculated by HFSS,CST and FUNSAFE on Fine Mesh with Hemispherical Computational Domain with the P2 Scheme in the Case of Patch Antenna ($\varepsilon_r = 2.2$)

To investigate the reasonability of the results we got, several different cases are run. In HFSS, three different computational domains are applied, and in CST, both time domain and frequency domain are simulated, and for FUNSAFE, both Silver-Muller boundary condition and PML are applied. To show the main lobe more clearly, the radiation patterns of H-place are plotted in rectangular coordinates. As shown in Fig. 37, the side lobes of different simulation results are not exactly the same, but the main lobes match each other well. Considering the -3dB beam width, one of the main characteristics of patch antennas, they are close for each simulation method. The behavior of effects of computational domain on radiation pattern will be explored in more details in future work.

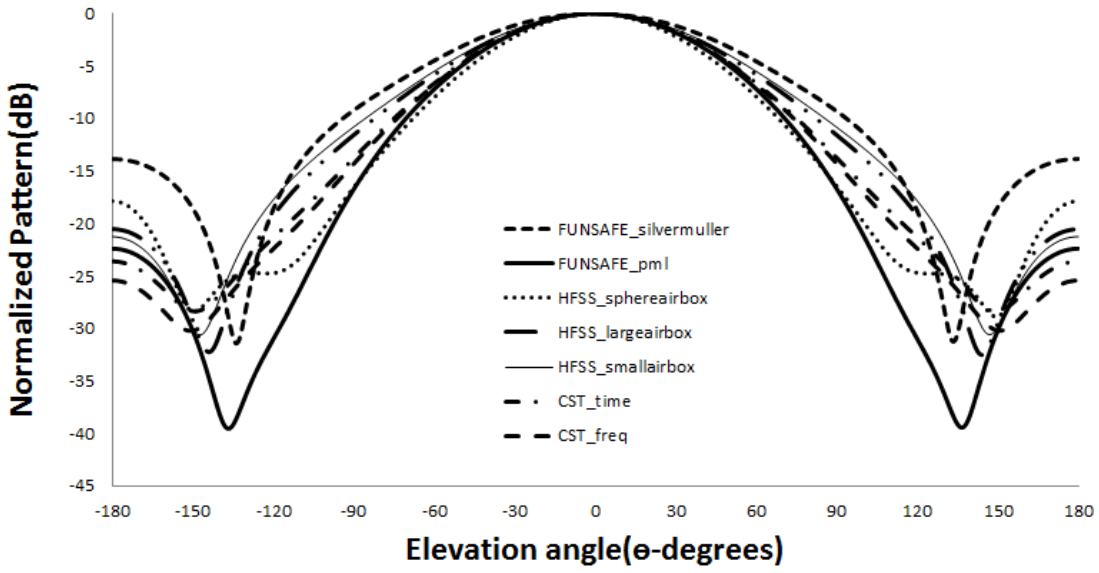

Figure 37 Comparison of Radiation Pattern (H-plane) at 2.35GHz Calculated by HFSS with Different Computational Domain, CST in Time-Domain and Frequency-Domain, and FUNSAFE with Different Boundary Conditions on Fine Mesh with Hemispherical Computational Domain with the P2 Scheme in Rectangular Coordinates in the Case of Patch Antenna ($\varepsilon_r = 2.2$)

CHAPTER V

CONCLUSION

A higher-order Petrov-Galerkin finite element method is applied in analysis of the antennas. Higher-order discretization is introduced in both spatial and temporal domains to solve Maxwell's equations. Implicit time stepping is applied in the time domain and quadratic elements are introduced in the mesh. Gaussian pulse is introduced as the excitation for the antennas which helps obtain frequency-based characteristics in one time-domain calculation.

To get antenna characteristics parameters including the scattering parameters, input impedance and radiation pattern, post processes are implemented. The theory and procedures of the post processes for antenna characteristics are discussed. The antenna characteristics obtained from the post processes are compared with the results of HFSS and CST for verification.

The first verification case is the monopole antenna. A quarter-wavelength monopole antenna fed by coaxial cable is simulated here. The working theory and characteristics of the monopole antenna are explained. Simulations are run on cases with different ground plane sizes to explore the effect of ground plane on antenna characteristics. The simulation results of FUNSAFE match well with HFSS. To test the grid convergence behavior, meshes with different sizes are applied with both p1 and p2 schemes. These results demonstrate that the p2 solution is significant more accurate than the p1 solution, even when the same number of degrees of

freedom are used. The effect of time-step size is also examined. The procedure of calculating input impedance is described in detail, and the results match well with those of HFSS.

The second verification case is the patch antenna. A rectangular patch antenna fed by coaxial cable is simulated here. The working theory and characteristics of the patch antenna are explained in detail. Simulations are run on cases with different permittivity of material in their substrates to explore the effect of substrate material on antenna characteristics. The simulation results are compared with theoretical results and results of HFSS and CST Microwave Studio. The grid convergence behavior is tested on meshes with different sizes which are applied with both p1 and p2 schemes. Simulation results on meshes with different distribution are discussed to show the importance of placing mesh points in appropriate locations and demonstrate the need for mesh adaption. Radiation patterns of the patch antennas are discussed with results from different simulation methods and different computational domains.

In future work, adaptive meshes will be introduced which will highly increase the efficiency of the simulations. Moreover, other feeding methods will be introduced to explore the capability of FUNSAFE to solve a wider variety of antennas, and other, more general, methods for calculating the input impedance will be developed which will help obtain the characteristics of the antennas fed by other models than the coaxial cable. In addition, the effect of computational domain on radiation patterns will be explored in more detail. Finally, a variety of antennas will be simulated by FUNSAFE for further verifications.

REFERENCES

[1] J. C. Maxwell, *A treatise on electricity and magnetism*. London,U.K.: Oxford Univ. Press, 1873.

[2] C. A. Balanis, "Antenna Theory - a Review," *Proceedings of the IEEE*, vol. 80, pp. 7-23, Jan 1992.

[3] S. Silver, *Microwave antenna theory and design*. New York,: McGraw-Hill Book Co., 1949.

[4] D. M. Pozar, D. Schaubert, and IEEE Antennas and Propagation Society., *Microstrip antennas : the analysis and design of microstrip antennas and arrays*. New York: Institute of Electrical and Electronics Engineers, 1995.

[5] K. Yee, "Numerical solution of initial boundary value problems involving Maxwell's equations in isotropic media," *Antennas and Propagation, IEEE Transactions on*, vol. 14, pp. 302-307, 1966.

[6] C. O. AMERICA, "CST STUDIO SUITE 2011: INTEGFRATING SIMULATION TECHNOLOGY," *Microwave Journal*, vol. 53, pp. 92-96, Dec 2010.

[7] R. F. Harrington, *Field computation by moment methods*. New York,: Macmillan, 1968.

[8] R. C. Hansen, *Moment methods in antennas and scattering*. Boston: Artech House, 1990.

[9] J. J. H. Wang, *Generalized moment methods in electromagnetics : formulation and computer solution of integral equations*. New York: Wiley, 1991.

[10] J.-M. Jin and D. J. Riley, *Finite element analysis of antennas and arrays*. Hoboken, N.J.: John Wiley & Sons : IEEE Press, 2009.

[11] V. Shankar, W. Hall, and A. H. Mohammadian, "A CFD-based finite-volume procedure for computational electromagnetics-interdisciplinary applications of CFD methods," in *9th AIAA Computational Fluid Dynamics Conference*, 1989, pp. 551-564.

[12] J. S. Shang and D. Gaitonde, "Characteristic-based, time-dependent Maxwell equation solvers on a general curvilinear frame," *AIAA journal*, vol. 33, pp. 491-498, 1995.

[13] J.-M. Jin, *The finite element method in electromagnetics*. New York: Wiley, 1993.

[14] ANSOFT, "HFSS(TM) 12.0: HIGH PERFORMANCE COMPUTING," *Microwave Journal,* vol. 52, pp. 118-120, Nov 2009.

[15] W. K. Anderson, L. Wang, S. Kapadia, C. Tanis, and B. Hilbert, "Petrov–Galerkin and discontinuous-Galerkin methods for time-domain and frequency-domain electromagnetic simulations," *Journal of Computational Physics,* vol. 230, pp. 8360-8385, 2011.

[16] A. N. Brooks and T. J. Hughes, "Streamline upwind/Petrov-Galerkin formulations for convection dominated flows with particular emphasis on the incompressible Navier-Stokes equations," *Computer methods in applied mechanics and engineering,* vol. 32, pp. 199-259, 1982.

[17] D. L. Bonhaus, "A higher order accurate finite element method for viscous compressible flows," *A higher order accurate finite element method for viscous compressible flows,* 1998.

[18] T. J. Barth, "Numerical methods for gasdynamic systems on unstructured meshes," in *An introduction to recent developments in theory and numerics for conservation laws*, ed: Springer, 1999, pp. 195-285.

[19] B. Cockburn, S. Hou, and C.-W. Shu, "The Runge-Kutta local projection discontinuous Galerkin finite element method for conservation laws. IV. The multidimensional case," *Mathematics of Computation,* vol. 54, pp. 545-581, 1990.

[20] C. A. Balanis, *Advanced engineering electromagnetics*. New York: Wiley, 1989.

[21] M. F. Iskander, *Electromagnetic fields and waves*. Englewood Cliffs, N.J.: Prentice Hall, 1992.

[22] P. L. Roe, "Approximate Riemann solvers, parameter vectors, and difference schemes," *Journal of computational physics,* vol. 43, pp. 357-372, 1981.

[23] F. Assous and E. Sonnendrücker, "Joly–Mercier boundary condition for the finite element solution of 3D Maxwell equations," *Mathematical and Computer Modelling,* vol. 51, pp. 935-943, 2010.

[24] S. G. Johnson, "Notes on perfectly matched layers (PMLs)," *Lecture notes, Massachusetts Institute of Technology, Massachusetts,* 2008.

[25] C. A. Balanis, *Antenna theory : analysis and design*, 3rd ed. Hoboken, NJ: John Wiley, 2005.

[26] "the IEEE Standard Definitions of Terms for Antennas(IEEE Std 145-1983)."

[27] J. A. Kong, *Electromagnetic wave theory*, 2nd ed. New York: Wiley, 1990.

[28] J. L. Volakis, *Antenna engineering handbook*, 4th ed. New York: McGraw-Hill, 2007.

[29] J. D. Kraus and R. J. Marhefka, *Antennas for all applications*, 3rd ed. New York: McGraw-Hill, 2002.

[30] R. C. Johnson, H. A. Ecker, and J. S. Hollis, "Determination of far-field antenna patterns from near-field measurements," *Proceedings of the IEEE*, vol. 61, pp. 1668-1694, 1973.

[31] J. G. Maloney, G. S. Smith, and W. R. Scott Jr, "Accurate computation of the radiation from simple antennas using the finite-difference time-domain method," *Antennas and Propagation, IEEE Transactions on*, vol. 38, pp. 1059-1068, 1990.

[32] J. G. Maloney and G. S. Smith, "A study of transient radiation from the Wu-King resistive monopole-FDTD analysis and experimental measurements," *Antennas and Propagation, IEEE Transactions on*, vol. 41, pp. 668-676, 1993.

[33] T. W. Hertel and G. S. Smith, "The insulated linear antenna-revisited," *Antennas and Propagation, IEEE Transactions on*, vol. 48, pp. 914-920, 2000.

[34] S. N. Makarov, *Antenna and EM modeling with Matlab*. New York: Wiley-Interscience, 2002.

[35] J.T.Bolljahn, "Antennas near Conducting Sheets of Finite Size," *Univ, California Dept. Eng. Rep.162*, 1949.

[36] J. E. Storer, "The impedance of an antenna over a large circular screen," *Journal of Applied Physics*, vol. 22, pp. 1058-1066, 1951.

[37] R. G. Kouyoumjian and P. H. Pathak, "A uniform geometrical theory of diffraction for an edge in a perfectly conducting surface," *Proceedings of the IEEE*, vol. 62, pp. 1448-1461, 1974.

[38] Z. Zivkovic, D. Senic, C. Bodendorf, J. Skrzypczynski, and A. Sarolic, "Radiation pattern and impedance of a quarter wavelength monopole antenna above a finite ground plane," in *Software, Telecommunications and Computer Networks (SoftCOM), 2012 20th International Conference on*, 2012, pp. 1-5.

[39] D. M. Pozar, *Microwave engineering*, 3rd ed. Hoboken, NJ: J. Wiley, 2005.

[40] O. El Mrabet, "High Frequency Structure Simulator (HFSS) Tutorial," 2006.

[41] R. Munson, "Conformal microstrip antennas and microstrip phased arrays," *Antennas and Propagation, IEEE Transactions on,* vol. 22, pp. 74-78, 1974.

[42] J. Howell, "Microstrip antennas," *Antennas and Propagation, IEEE Transactions on,* vol. 23, pp. 90-93, 1975.

[43] A. Derneryd, "Linearly polarized microstrip antennas," *Antennas and Propagation, IEEE Transactions on,* vol. 24, pp. 846-851, 1976.

[44] Y. Lo, D. Solomon, and W. Richards, "Theory and experiment on microstrip antennas," *Antennas and Propagation, IEEE Transactions on,* vol. 27, pp. 137-145, 1979.

[45] M. Deshpande and M. Bailey, "Input impedance of microstrip antennas," *Antennas and Propagation, IEEE Transactions on,* vol. 30, pp. 645-650, 1982.

[46] E. O. Hammerstad, "Equations for microstrip circuit design," in *Microwave Conference, 1975. 5th European*, 1975, pp. 268-272.

[47] Y. T. Lo and S. W. Lee, *Antenna handbook : theory, applications, and design*. New York: Van Nostrand Reinhold, 1988.